Hydro-mechanical interactions of a rock slope with a retreating temperate valley glacier

Marc Hugentobler[1], Jordan Aaron[1], Simon Loew[1], Clément Roques[1,2]

1: Department of Earth Sciences, Engineering Geology, ETH Zurich, 8092 Zurich, Switzerland.

2: Centre for Hydrology and Geothermics (CHYN), Université de Neuchâtel, Neuchâtel, Switzerland.

Corresponding author: Marc Hugentobler (marc.hugentobler@erdw.ethz.ch)

Highlights

- We monitored subsurface pore pressures and micrometer scale strain in a rock slope during glacial retreat
- Pore pressures are controlled by effects from snowmelt and rainfall infiltration and the connectivity to the englacial hydrological system
- We identified thermo-hydro-mechanical drivers for reversible deformation and irreversible rock mass damage acting at various timescales

Abstract

Rock slope failures often result from progressive rock mass damage which accumulates over long timescales, and is driven by changing environmental boundary conditions. In deglaciating environments, rock slopes are affected by stress perturbations driven by mechanical unloading due to ice downwasting and concurrent changes in thermal and hydraulic boundary conditions. Since in-situ data is rare, the different processes and their relative contribution to slope damage remain poorly understood. Here we present detailed analyses of subsurface pore pressures and micrometer scale strain time series recorded in three boreholes drilled in a rock slope aside the retreating Great Aletsch Glacier (Switzerland). Additionally, we use monitored englacial water levels, climatic data, and annually acquired ice surface measurements for our process analysis. Pore pressures in our glacial adjacent rock slope show a seasonal signal controlled by infiltration from snowmelt and rainfall as well as effects from the connectivity to the englacial hydrological

system. We find that reversible and irreversible strains are driven by hydromechanical effects from diffusing englacial pressure fluctuations and pore pressure reactions on infiltration events, stress transfer related to changing mechanical glacial loads from short-term englacial water level fluctuations and longer-term ice downwasting, and thermomechanical effects from annual temperature cycles penetrating the shallow subsurface. We relate most observed irreversible strain (damage) to mechanical unloading from ice downwasting. Additionally, short-term stress changes related to mechanical loading from englacial water level fluctuations and hydromechanical effects from pore pressure variations due to infiltration events were identified to contribute to the observed irreversible strain.

Plane language summary

The formation of rock slope instabilities is a long-term process related to continuous rock mass weakening driven by different environmental drivers. For rock slopes in glaciated valleys, increased rates of rock mass damage are assumed to occur during ice retreat due to a reduction of the glacier weight and concurrent changes in rock temperatures and slope groundwater pressures. However, because direct field measurements are missing, the effects of warm, retreating valley glaciers on groundwater pressures and progressive rock mass damage in adjacent rock slopes are still poorly understood. Here we present detailed analyses based on new borehole monitoring data and glacial water level measurements to improve the understanding of the involved processes. We find that the glacial hydrology influences the dynamics of the groundwater pressures in the adjacent rock slope at timescales from days to years. We record micrometer-scale reversible (elastic) deformation and irreversible rock mass damage and identify the involved drivers, such as rock slope groundwater pressure fluctuations, annual surface temperature variations, and changes in glacial loads. All these processes are identified to contribute to progressive rock mass weakening at different timescales and magnitudes, while we relate most of the observed damage to mechanical unloading from ice downwasting.

Keywords

Rock slope deglaciation; groundwater recharge; englacial pressure variation; borehole strain; progressive rock mass damage; paraglacial rock slope evolution

1. Introduction

Large rock slope instabilities develop through progressive rock mass damage during thousands of years driven by various transient environmental loads. In deglaciating environments, increased rates of damage are expected (Ballantyne et al., 2014; Grämiger et al., 2017; McColl, 2012; Riva et al., 2017), caused by stresses related to ice downwasting in combination with increased dynamics in the thermal and hydraulic boundary conditions acting on ice-free slopes (Grämiger et al., 2020). While the degree at which a slope reacts to changing environmental boundary conditions strongly depends on its predisposition and state of damage (i.e., rock mass strength, discontinuity properties and orientations, local stress state) (e.g., Cody et al., 2020; Gischig et al., 2016), the relative contributions of the different drivers to progressive rock mass damage during ice retreat remains poorly known.

Until now, progressive rock mass damage in paraglacial environments has mainly been investigated through conceptual approaches and numerical models (Baroni et al., 2014; Grämiger et al., 2017; Grämiger et al., 2018; Grämiger et al., 2020; Riva et al., 2017; Spreafico et al., 2020). Most of these studies rely on assumptions regarding the mechanical, hydraulic and thermal properties, processes and boundary conditions that so far could rarely be verified because of lack of in-situ subsurface data. This paper is part of a long term research project, where we investigate these critical unknowns by setting up surface and subsurface monitoring systems on rock slopes adjacent to the tongue of the Great Aletsch Glacier (Hugentobler et al., 2020). While in a companion paper (Hugentobler et al., 2021) we have described and analyzed the thermal and thermo-mechanical drivers, here we focus on hydraulic and hydro-mechanical processes in a paraglacial environment at borehole and slope scale. We aim at specifically exploring the relative contributions of processes responsible for micrometer-scale borehole strain, such as rock slope and englacial pore pressure transients, longer term glacial ice downwasting, and the corresponding hydromechanical effects.

While “glacial debuttressing”, i.e., loss of horizontal support due to ice retreat has often been used to describe causes for slope failure, this concept has been called into question mainly because ice behaves viscous at low strain rates (Schulson, 1990) and therefore cannot build a strong buttress (McColl and Davies, 2013; McColl et al., 2010). Nevertheless, downwasting ice is understood to destabilize adjacent slopes due to a reduction of normal load on the toe of a landslide that reduces friction along discontinuities in the rock

mass (Wyllie and Mah, 2004). However, the significance of these changes in normal load are poorly constrained, mainly because some of the ice weight is compensated by buoyance effects during times of high englacial water pressures in temperate glaciers, and unknown coupling to the slope groundwater pressure (McColl et al., 2010).

Englacial water pressures of temperate glaciers show strong variations at diurnal to annual timescales (e.g., Fudge et al., 2005; Harper et al., 2005; Iken et al., 1996; Sugiyama and Gudmundsson, 2004). In contrast to reduced glacial loads with high englacial water pressures, quick increase of englacial water levels might also exert an additional load on the slope if these fluctuations occur at a rate that is faster than the englacial hydrological system can equilibrate with the slope groundwater.

The transient englacial hydrological system of temperate valley glaciers can be subdivided into two season-dependent end-member systems (Fudge et al., 2005). The summer system is characterized by strong daily water pressure fluctuations within a channelized drainage system driven by daily meltwater infiltration cycles and a relative low mean water pressure in areas that are not directly connected to the main drainage network (Fudge et al., 2005; Harper et al., 2005). Water pressure measurements in glacial boreholes have shown that pressure fluctuations can have amplitudes from nearly ice overburden pressure down to atmospheric values in the main drainage conduit and directly connect channels. The amplitudes of pressure variations decay laterally in the glacial ice within a few tens of meters distance from the connected channel (Hubbard et al., 1995). In wintertime, the efficient drainage system of the summer ceases and a linked-cavity based system establishes causing relatively constant high water pressures within the glacier at a level close to ice overburden (Harper et al., 2005; Lappegard et al., 2006).

These variations in pressure within the glacier may diffuse into the adjacent rock slopes if both are connected through permeable structures. It is often assumed that a temperate glacier imposes a constant head boundary to the adjacent slope similar to the effect of a reservoir lake, and hence, that the slope hydraulic head is tightly linked to the glacial ice elevation (McColl et al., 2010). However, this might be an oversimplification, since englacial water pressures show strong temporal and spatial pressure variations and the ice-bedrock contact might be sealed with fine-grained basal till. The rate at which englacial pressure variations

propagate into the slope is also a function of the hydraulic properties of the adjacent rock mass (i.e., hydraulic diffusivity), and the connectivity to the englacial hydrological system.

Hillslope bedrock hydrology also shows strong dynamics, related to temporal variations in recharge and storage-discharge functions (Fan et al., 2019; Kirchner, 2009). Phreatic groundwater levels in Alpine rock slopes normally show a seasonal signal (de Palézieux and Loew, 2019) with amplitudes dependent on the ratio between infiltration (from snowmelt and summer rainfalls) and the hydraulic diffusivity of the rock mass (Gleeson and Manning, 2008). Hydraulic properties in crystalline rocks are controlled by complex network of fractures organized within a relatively low permeability intact rock matrix (Singhal and Gupta, 2010). Hence, hydraulic properties are dependent of fracture density, connectivity, initial aperture, filling, and stress conditions (Lavoine et al., 2020; Maillot et al., 2016). It is often observed that hydraulic conductivity and storage show a non-linearly decreasing trend with depth due to increasing overburden stress (Achtziger-Zupančič et al., 2017; Manning and Ingebritsen, 1999). Increased fracture density and interconnectivity at the shallow subsurface can result in unconfined behavior of fractured rock aquifers, whereas at greater depth with less interconnected fractures, a higher degree of confinement is regularly observed (Kaehler and Hsieh, 1994; Rahi and Halihan, 2013; Welch and Allen, 2014).

Earth and atmospheric tides also have a measurable impact on subsurface pore pressure dynamics (Acworth et al., 2016; Hsieh et al., 1987). Earth tides are caused by gravitational fluctuations related to the movement of celestial bodies relative to Earth and result in poroelastic crustal deformation, causing variations in pore pressures (McMillan et al., 2019). Atmospheric tides result from variations in barometric pressure related to thermal expansion and gravitational effects (Chapman and Westfold, 1956).

It has been shown that dynamics in hydrological behavior may have a strong impact on slope movement and instability, especially through long-term cyclic loading and fatigue. Hydromechanical effects driven by pore pressure changes can cause reversible (elastic) deformation in stable rock slopes (Guglielmi et al., 2005; Hansmann et al., 2012; Rouyet et al., 2017). In unstable slopes, pore pressure increases are often identified as main drivers for acceleration (Bonzanigo et al., 2007; Groneng et al., 2011; Guglielmi et al., 2005; Huang et al., 2018; Loew et al., 2017; Preisig et al., 2016; Wolter et al., 2020). These processes also promote progressive rock mass damage due to subcritical crack-growth and are considered as important

preparatory factors for future rock slope instabilities (Guglielmi et al., 2008; McColl, 2012; Prager et al., 2008; Preisig et al., 2016; Riva et al., 2017).

Irreversible strain measured in rock slopes is often used as a proxy for rock mass damage, which in fractured rock masses comprise tensile or shear fracture propagation and breakage of intact rock bridges, degradation of asperities, and smoothing of discontinuities caused by fracture slip (Eberhardt, 2008; Gischig et al., 2011b; Grämiger et al., 2020; Preisig et al., 2016). Besides the magnitude of the hydromechanical loading (or load of any other origin), the strain reaction of a rock slope strongly depends on the rock mass properties (mainly degree of damage) and the spatially varying in-situ stress states. Stress concentrations in rock slopes are controlled by the slope geometry and the presence of discontinuities (joint networks and faults) at different spatial scales (Gischig et al., 2011a, b; Stock et al., 2012; Styles et al., 2011; Wolters and Müller, 2008; Young and Ashford, 2008).

Dependent on the criticality of the fracture system, a stress perturbation of a specific magnitude will either cause mainly elastic (reversible) strain if it lies below the fatigue limit, cause slow, subcritical fatigue crack growth if it lies above the fatigue limit, or even triggers quicker strain reactions if it locally reaches critical stress levels (Brain et al., 2014). Numerical simulations propose that hydromechanical stress changes related to pore pressure variations, in combination with changing mechanical loading due to ice fluctuations, are stronger drivers for progressive rock mass damage compared to purely mechanical unloading or thermomechanical stress changes in combination with ice fluctuations (Grämiger et al., 2017; Grämiger et al., 2018; Grämiger et al., 2020). These authors further show that besides long-term changes (hydromechanical and thermomechanical effects due to glacial cycles, and glacial loading and unloading cycles), seasonal thermomechanical and hydromechanical cycles are critical for generating irreversible rock slope deformation or damage.

In this study we present data and detailed analyses of pore pressure and micrometer scale strain time series recorded in three, 50 m deep boreholes, drilled in fractured crystalline rock at the margin of the rapidly retreating Great Aletsch Glacier (Valais, Switzerland). Climatic data and englacial water levels monitored in a nearby sinkhole enable us to investigate their effects on groundwater dynamics in our rock slope and the connectivity to the englacial hydrological system. Multi-annual and highest resolution multi-level axial and

158 radial strains monitored in our boreholes are compared to transient pore pressures, englacial water pressure
159 variations, and decreasing glacial ice levels. We investigate these mechanical and hydromechanical re-
160 sponses and discuss the dominant drivers for reversible deformation and irreversible rock mass damage on
161 time scales ranging from hours to years.

162 1.1. Site description

163 Our study site is located in fractured crystalline rock along the retreating glacier tongue of the Great Aletsch
164 Glacier (Valais, Switzerland) (Fig. 1). Bedrock outcrops along our approximately 30° dipping and NNW fac-
165 ing rock slope are glacially smoothed, and a distinct valley parallel ridge and furrow morphology is present.
166 The study site is located in the Aare-Massif (Steck, 2011), and the dominant lithologies consist of gneiss
167 and granites that form the ridges, and weaker schist layers or brittle-ductile shear zones following the alpine
168 foliation that normally form the furrows. The alpine foliation strikes valley parallel and is normally steeply
169 dipping into the slope. Three persistent joint sets are present at the study site showing normal spacings of
170 around 1 to 3 m at the ground surface and a decrease with depth (Hugentobler et al., 2020). The most
171 persistent joint set is foliation parallel, a second joint set is steeply SSW dipping, and the third persistent
172 joint set shows a slope subparallel orientation. The lower study area is covered by a recent, thin, and patchy
173 till layer containing several rock outcrops.

174 A number of active and relict/dormant rock slope instabilities occur in the region of the current glacier tongue
175 of the Great Aletsch Glacier (Grämiger et al., 2017). As visible on the map (Fig. 1), a few hundreds of meters
176 SW of our study site the well monitored and documented active Moosfluh rock slope instability is located
177 (Glueer et al., 2020; Glueer et al., 2019; Kos et al., 2016; Strozzi et al., 2010).

178 The extent of the Great Aletsch Glacier is well documented since the Little Ice Age (LIA) maximum, which
179 occurred around 1860 (GLAMOS, 1881-2019). This data shows an increased melting rate in more recent
180 years. Since the LIA, the glacier tongue has lost approximately 300 m of ice height at our study site, and
181 high-resolution surface models of the Great Aletsch Glacier from the years 2012 to 2020 show annual ice
182 height losses of around 10m per year (see Fig. 8, source: Swiss Federal Office of Topography).

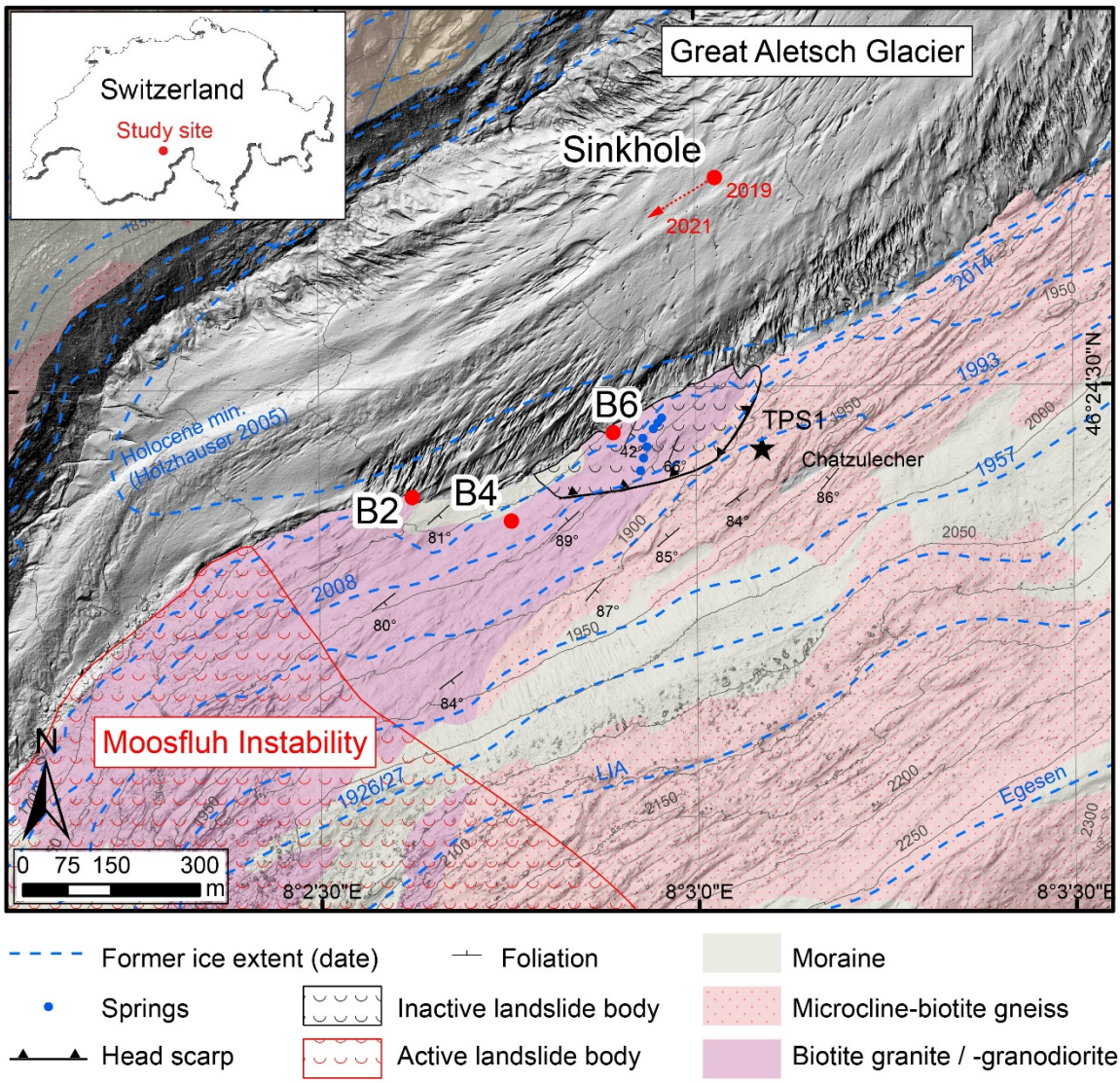

Fig. 1. Overview map showing the locations of the three boreholes B2, B4, and B6 aside the glacier tongue of the Great Aletsch Glacier (modified after Hugentobler et al., 2020) and the approximate location of the monitored glacial sinkhole. Ice extents from years 1927 to 2014 were digitized from historical aerial photos by Glueer et al. (2020). LIA (little ice age) and Egesen stadial ice extents are constraint by lateral moraines in the area of the map. The geological map from Steck (2011) was extended in areas that were ice covered during their mapping campaign.

1.2. Previous work

In summer 2017, a subsurface monitoring system containing three highly instrumented boreholes was installed beside the retreating glacier tongue of the Great Aletsch Glacier. The setup and performance of this system is described in Hugentobler et al. (2020) in detail. It consists of three ~ 50 m deep research boreholes

that were placed with variable lateral distance to the 2017 ice margin (Fig. 1) and at locations with variable rock mass quality. The boreholes are each 10 cm in diameter and were logged with geophysical and hydro-geophysical probes prior to the sensor installation. The boreholes were fully grouted after the permanent monitoring system had been installed. For a summary of the logging results refer to Hugentobler et al. (2020). All boreholes contain a temperature sensor chain with 1 m downhole spacing, a pore pressure sensor installed at the borehole end, an SAA in-place inclinometer chain with 0.5 m segment length to measure horizontal displacements, and a series connection of ten FBG sensors of approximately 5 m base length to measure the axial strain along the whole borehole length (Hugentobler et al., 2020).

The three boreholes were placed between 1 m and 50 m from the 2017 ice margin. One of the borehole locations, B6, was drilled in a former toppling rock slope instability that currently shows low activity (Fig. 1). This instability was identified by its distinct morphology with a head scarp, an outward rotated foliation, and more disturbed rock mass below (Geological Strength Index (GSI) values between 50 and 60) (Hugentobler et al., 2020). The other two boreholes were drilled at locations showing no signs of active or former slope movements and feature differences in rock mass quality (i.e., GSI values at B2 from 55 – 65 and at B4 from 75 to 85). Borehole pumping and infiltrations test results provide the following transmissivity estimates: ~10^{-6} m^2/s in the lower part of B2 and in borehole B4; ~10^{-3} m^2/s in the upper 15 m of B2, and ~10^{-5} m^2/s in B6, with higher assumed values at shallow depth.

2. Methods

2.1. Borehole monitoring systems

In this study we focus on the pore pressure, and axial (vertical) and radial (horizontal) strain measurements, collected at hourly intervals. Boreholes B4 and B6 are equipped with piezo-resistive pressure sensors (PA-27XW 10 bar by Keller AG with an accuracy below 2 mbar) installed in a 1 – 2 m long sand filter at 43.75 (B4) and 48.75 (B6) meters below ground surface. The pressure sensor in B2 was presumably damaged during grouting. The absolute pressure readings from the borehole sensors were corrected for atmospheric pressure variations using data from a pressure sensor installed at the study site (at TPS1 location, see Fig. 1).

Horizontal deformation is monitored with in-place inclinometers (SAAF500-003 by Measurand Inc.) that consist of accelerometer-based sensor arrays installed on rigid 0.5 m long segments separated by flexible joints. Temperature sensors, installed with 1 m spacing, are used for internal correction of temperature related variations in segment length. Vertical strain along the borehole is recorded by temperature corrected, pre-strained FBG (Fiber Bragg Grating) strain sensor chains (SC-01 by Sylex Fiber Optics s.r.o.) of approximately 5 m base-length. To improve the measurement precision, static hourly strain measurements are gained by measuring for around 30 s every hour and averaging the recorded strain. In Hugentobler et al. (2020) we show that the installed strain monitoring system can reliably detect vertical elongations/compressions strains with a precision of below 1 με (~ 4 μm) for the FBG sensors of 4 to 5 m base-length, and horizontal displacements with a precision of around 0.1 mm for the in-place inclinometer sensors with 0.5 m segment length.

Pore pressure and horizontal deformation (SAA in-place inclinometer) time series have been nearly continuously recorded since early October 2017 with only a few gaps of some days to a few weeks of duration related to battery issues. Vertical strain time series measured by the FBG system are reliably recorded since July 2018. A data gap from April to July 2018 that exists in all sensors of borehole B2 is related to a temporary glacier re-advance that overrun the borehole location and disrupted the sensors from the data loggers. All borehole monitoring systems (data loggers, power supply and transmission) were dismantled in summer 2021.

2.2. Glacial sinkhole pressure measurements

In August 2019, we installed a piezo-resistive pressure sensor connected to a datalogger (PAA-36XiW with GSM-2 logger by Keller AG) in a glacial sink hole at around 40 m depth. This sensor functioned until January 2021 but only recorded clear water pressure variations until April 2020. The glacial water pressure sensor is corrected for atmospheric pressure fluctuations, has a measurement accuracy of 3 mbar, a measurement interval of 10 min, and had a daily data transmission.

2.3. Time series analysis of head fluctuations

As will be shown in Section 3, the pore pressure monitoring time series contains high frequency signals of

> 1 cycle per day (cpd). We hypothesize three potential causes of these signals: 1) atmospheric pressure fluctuations, 2) earth tides and 3) slope hydraulic response to englacial pressure head fluctuations. To test these hypotheses, we applied filter techniques and spectral analysis. First, we used a high pass filter to extract frequencies greater 1 cpd. We then applied a fast Fourier transformation (fft) to detect the frequency bands at which cyclic signals occur.

The resulting amplitude spectra from the pore pressure sensors in the boreholes were compared to those expected for the three potential causes detailed above. To test whether atmospheric pressure or earth tides are the cause, we compared the fft results of the pore pressure sensors to the calculated amplitude spectra for the atmospheric pressure sensor at the study site and computed earth tides in the study area using the software TSoft (Van Camp and Vauterin, 2005). Additionally, we fit tidal components from earth and atmospheric origin to our continuous pore pressure data using the MATLAB's Tidal Fitting Toolbox. A comparison of the relative amplitude of earth and atmospheric tides contained in the pore pressure signal allows for the interpretation of the degree of confinement of an aquifer (Rahi and Halihan, 2013). Finally, we explored potential glacial control on these signals by computing the time lag between pressure fluctuations in the glacial sinkhole and the rock slope. For this we use a moving window cross-correlation MATLAB function (Marwan, 2020) with overlapping windows of 24 h length.

2.4. Pore pressure diffusion

Pressure diffusion in continuum type aquifers is regulated by the hydraulic diffusivity of the media, D = T/S = Kb/S (m^2/s), where S is the dimensionless storage coefficient that in a confined aquifer is defined as $S=bS_s$, where b is the aquifer thickness and S_s is the specific storage. T is the transmissivity of the aquifer (m^2/s) and K the hydraulic conductivity (m/s).

To investigate the relationship between diurnal pressure cycles measured in the glacial sinkhole and diurnal pressure head fluctuations in the boreholes, we use an analytical solution for one-dimensional pressure diffusion of a sinusoidal head boundary in a semi-infinite confined aquifer (Eqn.1, e.g., Zhou, 2008, and references therein). This equation shows that the sinusoidal head signal imposed at the boundary occurs at a distance x from the boundary with a reduced amplitude (damping) and a phase shift (time lag) effect. Eqn.

2 shows that the lag time (t_L), i.e., the time needed for the signal to diffuse from the source (here the subglacial drainage channel) to a given point in the slope, is proportional to the distance x from the point to the source and proportional to $\sqrt{S/T}$ $\left(=\sqrt{1/D}\right)$.

$$H(x,t) = H_0 e^{-x\sqrt{\pi S/t_0 T}} \sin\left(2\pi t/t_0 - x\sqrt{\pi S/t_0 T}\right) \quad (1)$$

$$t_L = x\sqrt{t_0 S/4\pi T} \quad (2)$$

H is the hydraulic head of the aquifer relative to a defined reference level (in m), x is the distance (m) to the boundary, and t is time. H_0 equals the amplitude of the sinusoidal head signal (in m) and t_0 the period of the oscillation.

Although, it is evident that pressure diffusion in crystalline rock is controlled by a complex network of fractures, our approach aims at estimating a bulk hydraulic diffusivity between the valley bottom, where the head fluctuation occurs (i.e., in the main subglacial drainage channel), and the borehole location close to the ice margin. The highly fractured near surface bedrock layer below the glacial ice (outside the subglacial drainage channel) is treated as a confined aquifer, the possibly unconfined section in the bedrock outside the glacier lateral margin is hereby neglected. The direct length between source and the monitoring borehole B4 is estimated to be 320m.

2.5. Strain data analysis

We use both the in-place inclinometer system (horizontal deformation) and the FBG system (vertical deformation) to investigate the deformation characteristics in our instrumented rock slope observed during glacial ice retreat. Because of the lower displacement resolution of the inclinometer system, it is mainly used to investigate the long-term irreversible displacement magnitudes, depth intervals and directions at the three borehole sites and is provided in Appendix B. The main analyses of the transient deformation processes from various drivers at different timescales are based on the higher-resolution FBG strain data. For these analyses we differentiate rapid strain events, that occur within the measurement interval of 1 hour, short-term strain events that occur within few hours to several days, and longer-term strain trends that are observed at time scales from month to years.

In section 3 and 4, we compare monitored pore pressures and FBG strain data from our boreholes. Changing mechanical (glacier) loads affecting the rock slope are transmitted through stress transfer into the rock mass, and therefore occur nearly immediately at the time of the load change. We hypothesize that rapid strain events might be driven by changing mechanical loads related to quickly changing water levels in the glacier and therefore compare our strain data to glacial sinkhole pressure data. Additionally, we investigate the timing of all rapid strain events occurring in the remaining period of the nearly 3-year long time series, where we do not have englacial pressure monitoring data. To investigate potential long-term effects of mechanical unloading due to ice downwasting, we compare annually retrieved glacial levels (source: Swiss Federal Office oof Topography), visualized in 2D cross-section through the three borehole locations, to the strain history of all FBG sensors.

We relate irreversible strain components to progressive rock mass damage (Hugentobler et al., 2021; Hugentobler et al., 2020). The differentiation between reversible and irreversible strain is not always trivial, because strain occurs in positive and negative direction and at different timescales. For the differentiation of strain signals at timescales of hours to a year, we compare the strain signals to the dynamics of the potential drivers for deformation (e.g., pore pressure, temperature). Strain that recovers after perturbation is defined as reversible and the portion of strain that remains after perturbation it is defined as irreversible. For longer-term strain trends, we discuss the displacement characteristics and potential drivers to define if it is interpreted as reversible or irreversible deformation.

3. Results and Interpretation

3.1. Englacial water pressure dynamics

We hypothesize that glacier head fluctuations are an important driver of high frequency head fluctuations in the adjacent rock slope in summertime. The pressures recorded by our sinkhole sensor at an initial depth of 40 m show englacial water level variations between August 8th, 2019 (start of the measurements) and April 28th, 2020 (Fig. 2c, Fig. 3c, h). During summer 2019, the pressure sensor measured atmospheric pressure values during nighttime and most of the day indicating that water level in the sinkhole must be below the sensor elevation. Only in the early afternoon pressure readings indicate a rise of the water level to elevations of ~ 5 to 20 m above the sensor (i.e., up to 20 to 35 m below ice surface). These diurnal signals

peak at the time of maximum surface temperatures and are only measured for a few hours a day (Fig. 2c, 3c). At some days pressure peaks also occur at other daytimes and coincide with rainfall events. During wintertime, pressure measurements indicate generally high englacial water pressures, often very close to the elevation of the ice surface, and some abrupt, low magnitude changes in water levels occur. After April 28th, 2020, the monitored pressure stayed constant at values close to atmospheric pressure for the rest of the sensors' lifetime (in January 2021) with only few, weak excursions.

We relate the diurnal pressure peaks in 2019 that occur in the afternoon to daily meltwater cycles that quickly fill the highly transmissive channelized englacial hydrological system, with which the monitored sinkhole presumably was connected during that period. We propose this because of the very constant diurnal signals measured over the whole summer season and no observed significant direct inflow into the sinkhole from supraglacial channels. The atmospheric pressure values and the absence of diurnal fluctuations in summer 2020 can be explained by a decoupling of the sinkhole from the englacial hydrological system probably due to ice movement. The hypothesized ice movement and trapping of the sensor is supported by the fact that it was not possible to retrieve the sensor anymore after this event. Such observed changes in hydrological response, also at a decameter-scale, are consistent with water pressure measurements made in boreholes of other temperate valley glaciers that only show strong pressure fluctuations (similar to our observed magnitudes), if they are directly connected to the englacial hydrological system (Fudge et al., 2005; Harper et al., 2005). Further, we relate sinkhole pressure peaks that coincide with rainfall events during summer 2019 to a quick filling of the englacial hydrological system by rainwater infiltration into the glacier (cf. Barrett and Collins, 1997) and possibly also increased glacial ice melting due to rainfalls. High englacial water levels measured during winter 2019/2020 agree well to the characterized winter mode of englacial hydrological system in literature (Fudge et al., 2005; Harper et al., 2005). The transition from the summer mode with diurnal pressure fluctuations to the winter mode observed in the sinkhole is characterized by an asymptotic approach to the steady high pressure wintertime value. This is consistent with transition characteristics measured by Fudge et al. (2005) in their boreholes classified as "Type 2". Abrupt changes in the steady wintertime water levels could be related to ice movement and related opening / closing of new flow paths (cf. Harper et al., 2005).

3.2. Long-term rock slope pore pressure dynamics

Fig. 2 shows pressure head variations in the two boreholes (panel a, b), pressure head measured in the glacial sinkhole (panel c), surface temperature measured at the study site and precipitation (provided by Swisstopo) (panel d). Pressure head variations in B4 show annual amplitudes from 15 to 20 m and have a clear seasonal cycle. The highest values are measured during springtime (indicated with a star symbol in Fig. 2) caused by annual snowmelt, followed by a long-term head recession over the rest of the year superimposed by smaller events arising from intense summer rainfalls. In late winter, pressure heads tend to approach annual minimum values around 10 ± 5 m, and might show a lowering trend over the years (e.g., no. 1 to 3 in Fig. 2a). In B6, a more damped signal is observed compared to B4 with a weaker seasonal amplitude of only 1 - 2 m. The difference in the hydrological signals measured in the two boreholes may be related to the differences in local fracture density, transmissivity and connectivity (cf. section 1.2). We assume that the increased transmissivity in the disturbed rock mass of the inactive slope instability around B6 causes an efficient draining of the surface layer at this borehole location and hence keeps the pressure head after regrouting the deformation sensors in summer 2018 relatively constant. Additionally, infiltration from a creek fed by springs located some decameters above the borehole is assumed to stabilize the pressure head in B6.

The unusual recession shape approaching a minimum head values in B4 in late winter (no. 1 to 3 in Fig. 2a) could be related to a constant head boundary effect of the temperate Aletsch Glacier during the winter season. In winter 2020 this cannot be observed because of some rainfall events during wintertime that caused rock slope infiltration. To support this hypothesis, we show the ice elevation of the lateral ice-rock contact, from a cross-section through B4, relative to the sensor depth in this borehole (Fig. 2a, dashed black line). In winter 2018 and 2019 the ice elevation line is a few meters above the minimum head value and in winter 2021, the line is about 10 m below the minimum value. The observation of water ponds at the glacier-slope contact exactly at the time of minimum head values in winter 2019 (no. 2, Fig. 2) were made during a maintenance visit. This shows that the hydraulic head in the glacier during this late wintertime can even be few meters above the glacier-slope contact line and provides support to our hypothesis.

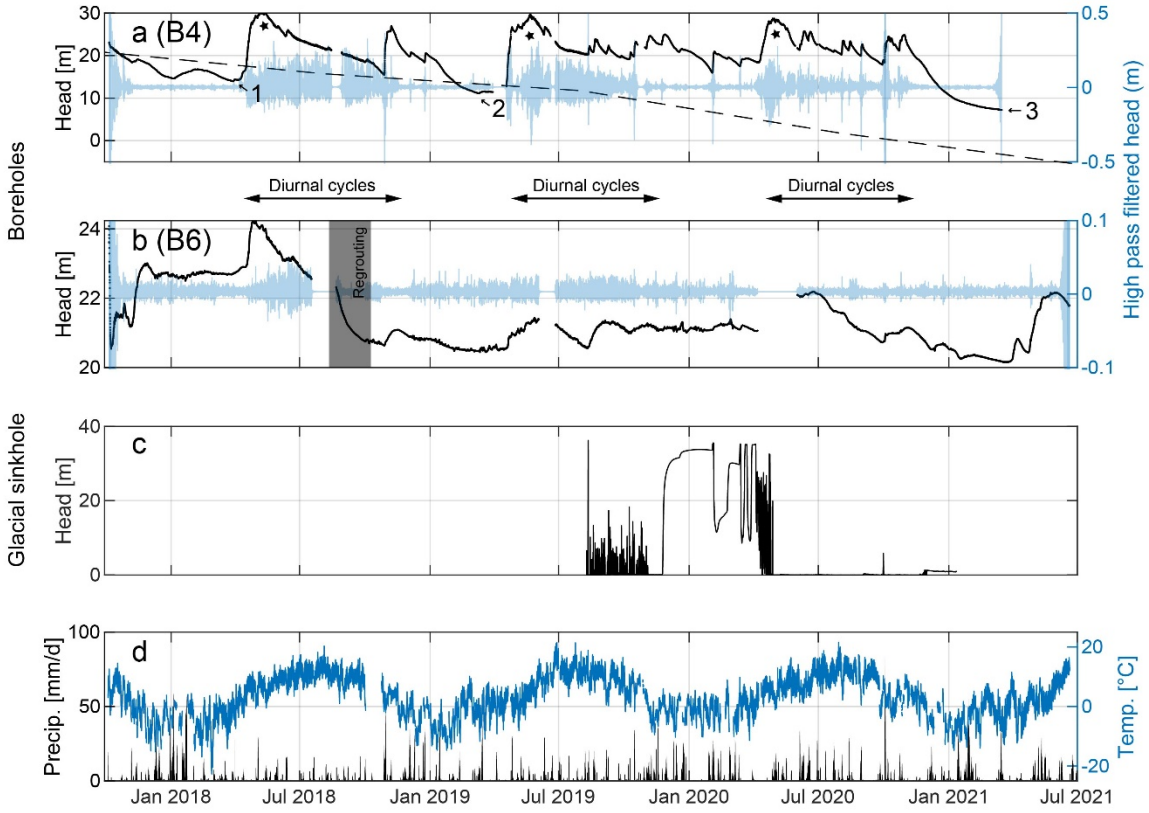

Fig. 2. a, b: Pressure head data of pore pressure sensors installed in borehole B4 at 43.75 m depth and in borehole B6 at 48.75 m depth. The dashed line in a illustrates the elevation of the ice level at the lateral ice margin below B4 relative to the pressure head elevation (similar as in panel b in Fig. 8) In blue, the high pass filtered pressure head data shows frequencies greater 1 cycle per day (cpd). The numbers and the star symbol in panel a are labels referred to in the text. c: Pressure head measured in the glacial sinkhole installed at approximately 40m depth (in year 2019) from August 2019 until January 2021. d: Cumulative total precipitation data (per 24 h) provided by MeteoSchweiz from the weather station "Bruchji" (Valais) located approximately 6 km away from our study site and surface temperature recorded locally at the study site.

3.3. Short-term rock slope pore pressure dynamics

3.3.1. Controls on high frequency pressure signals

During the summer season, diurnal head fluctuations are superimposed on the seasonal pressure head variations discussed in the previous section. The occurrence of these diurnal fluctuations in the time series

390 is illustrated by the magnitude of the high pass filtered head in Fig. 2(a, b), which visualizes frequencies
391 larger than 1 cycle per day (cpd). These fluctuations are observed in both boreholes (see Fig. 3a, b), but
392 the pressure head amplitude of the signal varies (~ 0.25 m in B4 and ~ 0.05 m in B6 in summer 2018 and
393 decreasing amplitude values down to approximately 1/3 in 2020). In both boreholes, the maximum values
394 occur in the afternoon. Fig. 3 also shows that during wintertime (December), although glacial dynamics
395 reached a steady state (Fig. 3 c), both boreholes still show cyclic signals at frequencies of 1 cpd and greater
396 but with a clearly lower amplitude (factor 2 to 10) with respect to the summer signals. The higher amplitude
397 summertime fluctuations in the slope cease simultaneously with the diurnal sinkhole fluctuations (observed
398 in November 2019; see Fig. 3).

399 As mentioned in the methods section, these high frequency pressure signals may be caused by a combina-
400 tion of earth tides, atmospheric pressure variations, and glacier head fluctuations. In Appendix A we present
401 the detailed investigation of this signal. We specifically aim at modeling the effect of Earth and atmospheric
402 tides in order to separate their effects from the one emerging from glacial head fluctuation. In addition, the
403 analysis also provides insights into the properties of the aquifer at the two borehole locations. Appendix A
404 shows that the wintertime high frequency signals (Fig. 3f, g) are likely caused by a combination of Earth
405 tides and atmospheric pressure variations. However, Appendix A also shows that Earth tides and atmos-
406 pheric pressure variations cannot explain the higher amplitude summertime diurnal signals. This indicates
407 a direct relationship of englacial and slope pressure head signals.

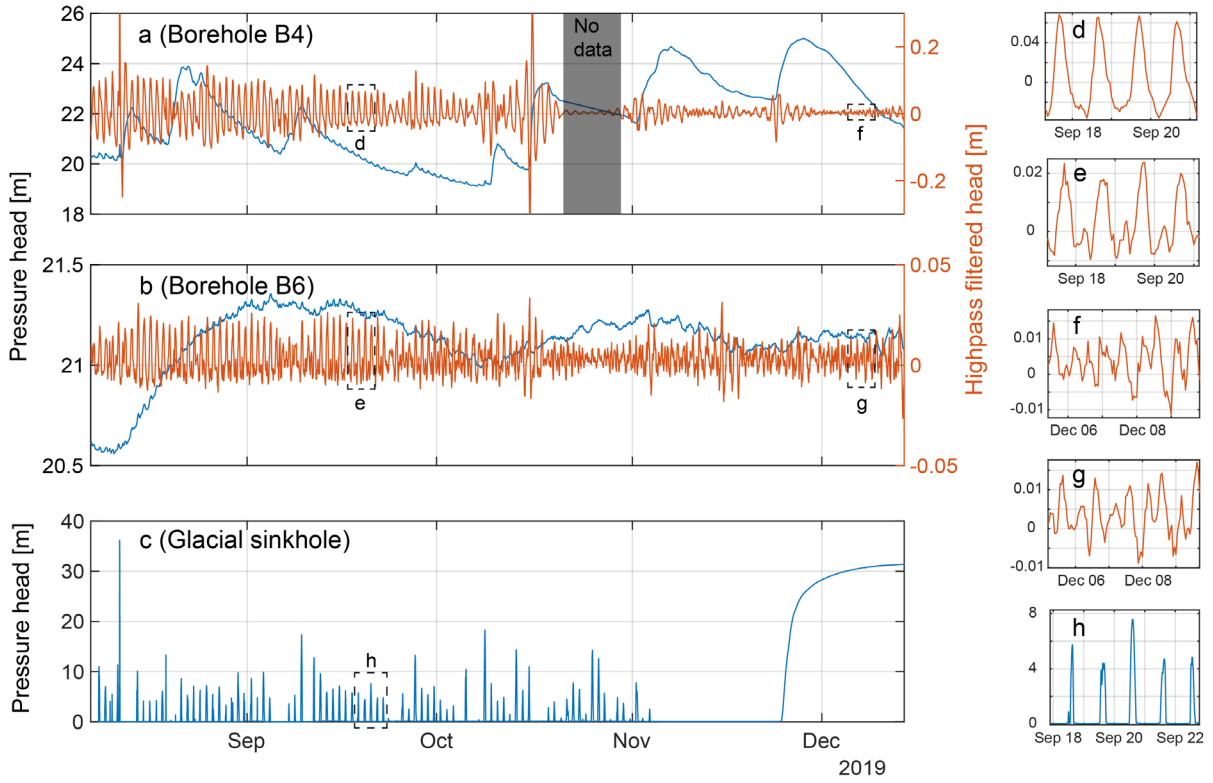

Fig. 3. Pressure head (blue lines) time series of borehole B4 (a) and borehole B6 (b) including high pass filtered data (orange lines) to visualize frequencies > 1 cpd contained in the data. In subpanel (c) is presented pressure head time series monitored in the glacial sinkhole between August and December 2019. Panels d-h show zooms on specific sequences of the pressure head data corresponding to the dashed black lines in subpanels a, b, and c.

3.3.2. Pore pressure diffusion between glacier and rock slope

As summarized in the previous section, there appears to be a strong correlation between glacier and slope pressure head fluctuations during summer and fall. In the present section we quantitatively analyze the correlation between these two signals, assuming that this correlation is controlled by pore pressure diffusion in the fractured bedrock. Signal analysis from borehole B4 suggest that the aquifer to the monitoring interval behaves as confined. This is supported by both the analysis of Earth and atmospheric tides (Appendix A) and the interpretation of borehole pumping test results (data not presented here) that show accurate predictions with transient pore pressure diffusion solutions assuming confined conditions, as classically observed for deeper fractured rock aquifers (Barker, 1988; Theis, 1935).

In Fig. 4 we compare the two signals for the borehole B4 location, with Fig. 4a showing the pressure peaks measured in the glacial sinkhole and the high pass filtered data of the pore pressure in B4. Panel b of Fig. 4 shows the pressure head measured in the borehole with the diurnal fluctuations superimposed to the long-term recessions. The temporal evolution in lag time between englacial and pore-pressure head signals considering data from B4, calculated based on the cross-correlation analysis described in Section 2.3, is provided in Fig. 4c. During recharge events, the computed lag-time shows negative excursions. The excursions are artifacts because no clear diurnal signals can be compared in the cross-correlation analysis, which is used to calculate the lag-time. This is because the high pass filtered borehole pressures are disturbed by the head rise due to infiltration and often no signals at all are detected during these times in the glacial sinkhole.

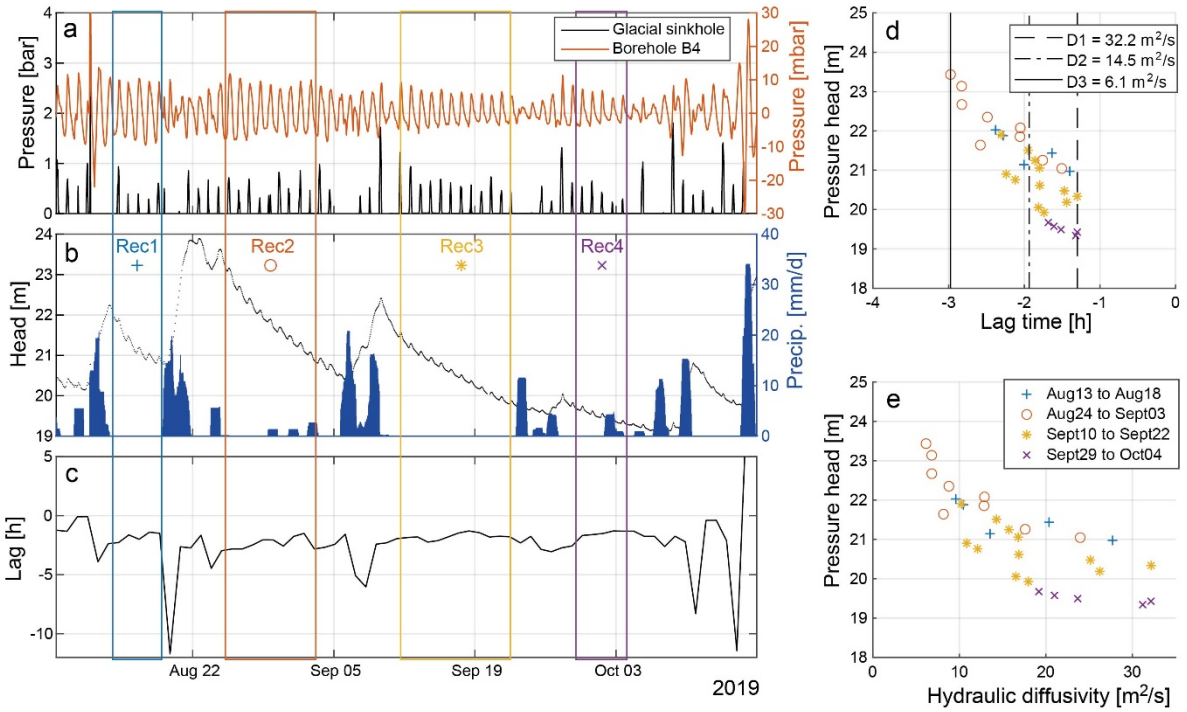

Fig. 4. a: Comparison of high pass filtered (> 1 cpd) borehole pore pressure data in B4 with pressure peaks measured in the glacial sinkhole. b: Pressure head data of borehole B4 and cumulative total precipitation data (per 24 h) provided by MeteoSchweiz from the weather station "Bruchji" (Valais). c: Lag time between the glacial pressure peak and the maximum of the diurnal pressure cycles in the borehole. d: Comparison of the daily mean pressure head in the borehole

with the lag time for the undisturbed pressure head recession sections indicated with Rec1 to Rec4 in b. e: Pressure head in the borehole versus hydraulic diffusivity calculated from the lag time value (using Eqn. 2).

Negative values in Fig. 4c indicate a clear delay of a few hours of the borehole pore pressure peaks compared to the glacial signal. During rain-free pressure head recession periods (Rec1 – Rec4, Fig. 4), we found that the lag time changes over time and decreases as the recession advances (Fig. 4c). Fig. 4d shows the daily mean pressure head as a function of the corresponding lag time computed for the four indicated recessions. This plot shows a clear linear relationship between both variables with a decreasing trend in lag time as pressure head decreases.

We further process this data to quantify the hydraulic diffusivity involved at different pressure heads and recessions (analytical solution provided in section 2.4). The range (mean, min., and max.) of hydraulic diffusivities is marked in Fig. 4d as vertical lines. Additionally, we provide in Fig. 4e the relationship between the mean daily pressure head and computed hydraulic diffusivity.

There are different options how the observed linear relationship on Fig. 4d can be explained. Either it reveals a transitory state in diffusivity (D) or flow path length/geometry (x) (see Eqn. 2). While a change in the heterogeneous pressure diffusion pathways in our fractured aquifer path might be possible, the modification in lag time is probably mostly controlled by changing diffusivity. This change could be caused by unsteady T or S in response to transitory hydraulic and/or mechanical conditions involved, as it has been shown in other studies (Elkhoury et al., 2006; Manga et al., 2012). For example, in confined aquifers a change in pressure head can cause hydromechanical deformation, e.g., fracture opening due to increased pore pressures. This can have an effect on both terms that control the hydraulic diffusivity (i.e., T and S) because of changes in the rock mass porosity.

We therefore hypothesize that the observed linear relationship between the lag time and the pressure head in the borehole is related to hydromechanical effects that cause changes in fracture aperture (i.e., change in rock mass porosity) and thus also change the hydraulic diffusivity. Hydromechanical effects related to pore pressure changes in the rock slope are addressed in section 3.4.3.

3.4. Hydromechanical couplings at diurnal, seasonal and decadal time scales

The high resolution vertical FBG strain data monitored in the three research boreholes allows for a detailed investigation of the different superimposed deformation processes that occur at various timescales and magnitudes. Raw data of the ten strain sensors installed in borehole B4 and B2 are shown in Fig. 5 and Fig. 7, respectively. Data of B6 is provided in Appendix C (Fig. C 1). Besides the strain time series that are plotted in the center of their anchoring depth interval, with FBG-1 being the shallowest sensor and FBG-10 the deepest, we additionally show the magnitude of the pressure head monitored in the corresponding borehole (for B4, B6; gray area) and precipitation data (lower panel). Fig. 7 of B2 strains additionally contains time series of the pressure measured in the glacial sinkhole for comparison.

We observe reversible (elastic) strain signals, strain signals that show both a reversible and irreversible component, as well as clearly irreversible strain signals. Reversible strain occurs e.g., on a diurnal cyclicity with magnitudes of about 5 με and can be detected in most deeper sensors during summertime (see indicated signals in Fig. 6a, and section 3.4.1). Reversible strain also occurs on an annual cyclicity, which can be clearly observed in the near-surface sensors FBG-2 and 3 of Fig. 5. According to the findings in Hugentobler et al. (2021) these annual strain cycles are related to thermoelastic strain in connection with annual surface temperature cycles penetrating the shallow subsurface.

Comparison of rapid (e.g., label a in Fig. 5) and short-term strain events (e.g., label b in Fig. 5) with potential drivers for deformation (e.g., precipitation events, pore pressure changes, temperature changes, and close earthquakes) revealed that the majority of these events coincide with precipitation or pore pressure changes (Hugentobler et al., 2021). Short-term strain events, further discussed in section 3.4.3, often show similarities in timing and duration with pressure head signals measured in the borehole and therefore are interpreted as hydromechanical effects driven by pore pressure fluctuations in fractures e.g., caused by rainfall or snowmelt infiltration (cf. Hugentobler et al., 2021). Rapid strain events manifest as steps in the time series, occur as both extension and shortening, typically show magnitudes of a few up to around 20 με, and often occur at several sensors simultaneously. We address the origin of these signals in section 3.4.2. Strain events that coincide with the timing of the seasonal switch of the englacial hydrological system are provided and discussed in section 3.4.4. Longer-term (at our multi-annual timescale) irreversible trends observed in the

491 strain time series (e.g., FBG-7 and FBG-10 in Fig. 5) and potential causes are discussed in section 3.4.5.

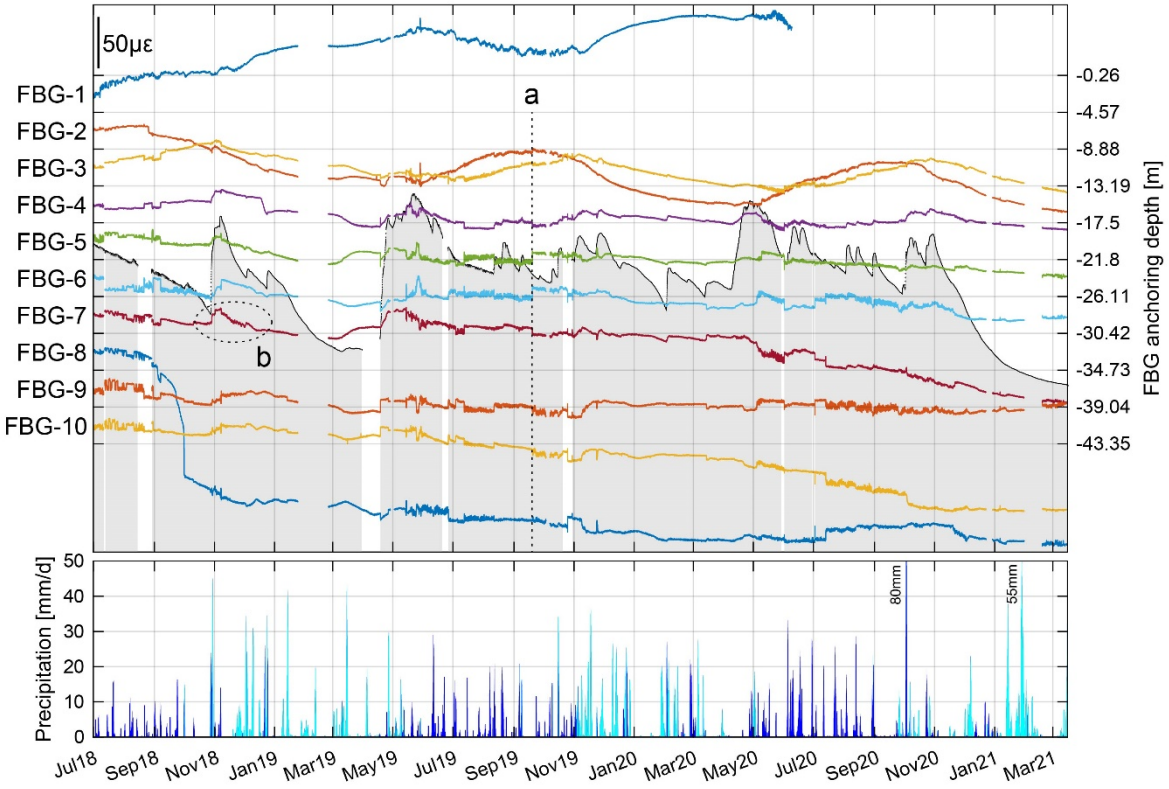

493 *Fig. 5. Temperature corrected FBG strain time series of individual 4.31 m base-length sensors installed in borehole B4*
494 *visualized after Hugentobler et al. (2021) with added data form winter/spring 2021. The strain data (colored lines) is*
495 *plotted at the center of the specific depth interval with anchoring depth labeled on the right side. Positive strain equals*
496 *axial extension and negative strain contraction. The strain scale is provided in the upper left corner in microstrain (μm/m).*
497 *The elevation of the pressure head is provided as a gray area in the background. Labels a and b indicate strain events*
498 *referred to in the text. The lower bar plot shows the cumulative total precipitation data per 24 h from the Bruchji weather*
499 *station (Valais) located approximately 6 km away from the study site (data provided by MeteoSchweiz). Cyan bars*
500 *indicate precipitation that probably occurred as snow (i.e., at surface temperatures below 1°C (Jennings et al., 2018)).*

501

502 In Fig. 6, the strain time series of the lower six sensors of borehole B4 are compared to pressure readings
503 from the glacial sinkhole sensor, the pressure head in the borehole, precipitation information, as well as

surface temperature data. Fig. 6a-c show the time series during summertime and Fig. 6d-f the winter season time series of the same sensors.

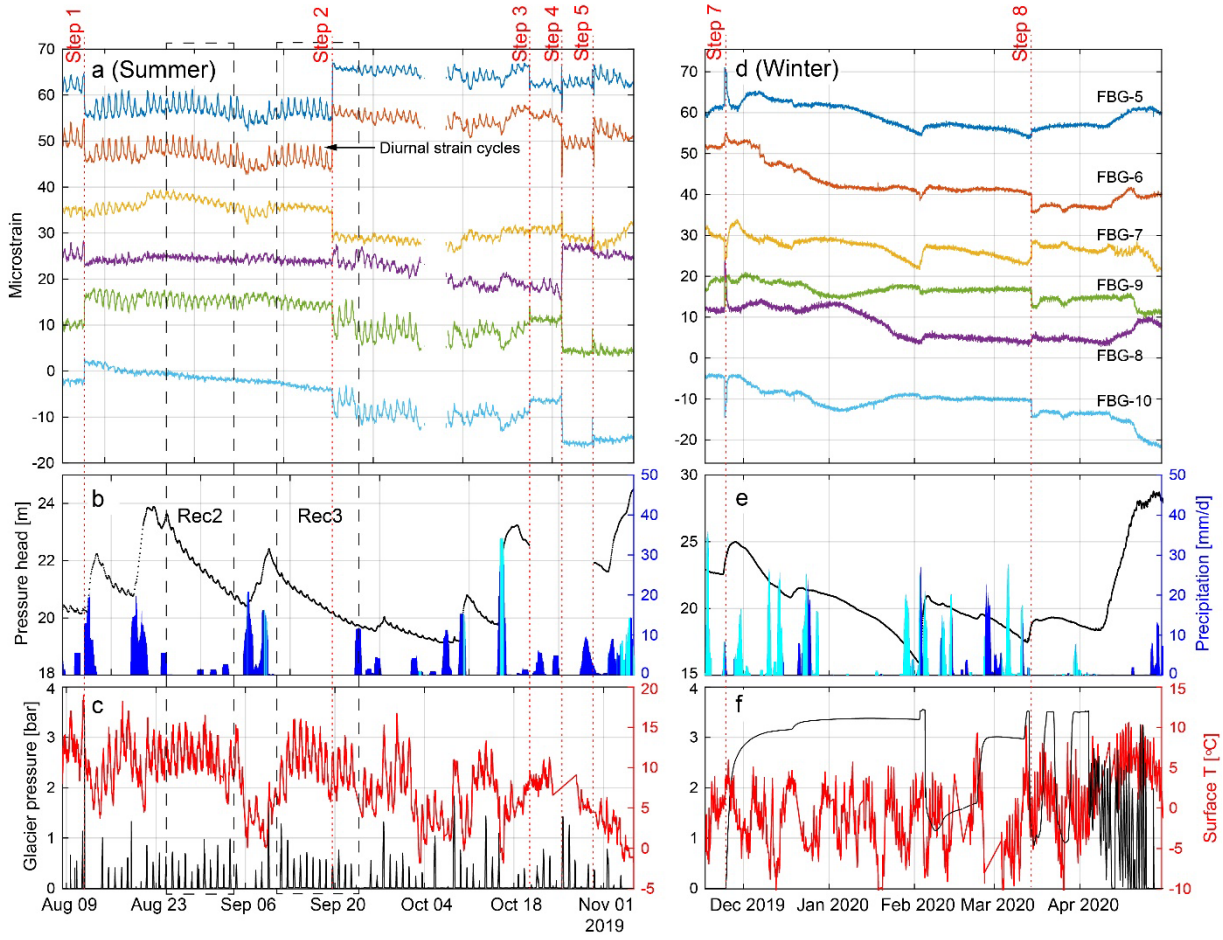

Fig. 6. a, d: FBG strain data (plotted with 10 με offset for better visualization) of the lower six sensors of B4 (FBG-5 to FBG-10) that are affected by pressure head changes during summer- and wintertime. b, e: Pressure head measured in borehole B4 at 43.75 m depth and Cumulative total precipitation data (per 24 h) provided by MeteoSchweiz from the weather station "Bruchji" (Valais). The cyan colored bars indicate precipitation that presumably occurred as snow (i.e., at surface temperatures below 1 °C at our study site (cf. Jennings et al., 2018)). c, f: Pressure measured in the glacial sinkhole at approximately 40 m depth and surface temperature measured at the study site.

3.4.1. Diurnal strain cycles

The comparison of the summer and winter time series shows that the diurnal strain fluctuations are only present during summertime (Fig. 6). This matches with the measurements made in the glacier and borehole

pressure sensors, as described above. Clear strain cycles only occur at sensor depths below the pressure head of the borehole (see Fig. 5 and Fig. C 1, Appendix C). These diurnal strain signals show a positive or negative correlation with diurnal pressure head cycles and start and stop at the same time in the year. According to the findings presented in section 3.3, we relate the diurnal fluctuations in the pressure head to glacial water pressure fluctuations driven by daily meltwater cycles that diffuse below the glacier into the rock slope aquifer. The strain cycles that occur simultaneously with diurnal pressure head fluctuations in the slope are understood as poroelastic effects driven by pressure fluctuations in transmissive fractures.

Strain sensors where the diurnal strain signal shows a positive correlation with the pressure head are interpreted to monitor at least one transmissive fracture in the interval (e.g., FBG-5, FBG-6, and FBG-7 between Step 1 and Step 2 in Fig. 6a). A negative correlation with pressure head (e.g., FBG-9 between Step 1 and Step 2 in Fig. 6a) can be explained by monitoring intervals that intersect unconnected open fractures that do not show strong pressure fluctuations. In this case, water pressure increase in fractures outside the interval can cause closing of the structure within the specific interval. Further, there are strain sensors that do not show diurnal fluctuations but are located below the pressure head in the borehole (e.g., FBG-8 and FBG-10 between Step 1 and Step 2 in Fig. 6a). This behavior can be explained by monitoring intervals that contain closed, unconnected fractures or intact rock. Similar observations have been made in experiments of the Grimsel Underground Test Site (Krietsch et al., 2020).

3.4.2. Rapid strain events

The rapid strain events indicated with red dashed lines in Fig. 6a show a temporal correlation with pressure peaks measured in the glacial sinkhole without any time delay. This is also the case for all the other rapid strain events that occurred in any of the three boreholes during the time when glacial pressure variations could be measured (i.e., between August 2019 to April 2020). Two specific rapid events of Fig. 6, one coinciding with a glacial pressure peak related to heavy rainfalls (Step 1) and one coinciding with an afternoon meltwater peak (Step 2), are illustrated in a zoom with increased temporal resolution in Fig. C 2 (Appendix C).

As mentioned above, we relate summertime pressure peaks measured in the glacial sinkhole to a quick filling of the channelized glacial hydraulic system due to diurnal glacial meltwater cycles or heavy rainfalls.

543 The highest glacial melting rates naturally occur at daily maximum temperatures in the afternoon. Because
544 these rapid strain events occur without any measurable time delay with glacial pressure peaks - and not
545 with a few hours delay from the glacial pressure diffusion to the B4 borehole location (Section 3.3.2) - these
546 strain steps cannot be explained by hydromechanical effects related to pore pressure diffusion.

547 We interpret these signals to be triggered by critical stress states in the slope, resulting from mechanical
548 loading of the glacier at high or low englacial water levels. The analyses of the timing of rapid strain events
549 shows that they either coincide with (1) daily maximum surface temperatures (i.e., filled englacial hydrolog-
550 ical system by meltwater), (2) heavy rainfall events (i.e., filled englacial hydrological system by rain and
551 rainfall induced meltwater), or sometimes with (3) daily minimum temperatures (i.e., empty englacial hydro-
552 logical system). The minority of rapid strain events that coincide with minimum daily temperatures often
553 show a reversed strain orientation compared to the previous rapid strain event. Because these rapid events
554 normally occur at several sensors simultaneously, we assume that they reflect a cascade of slip events
555 triggered in the fracture network. The rapid events do not occur at every extreme loading stage (Fig. 6). We
556 propose that this is related to a cyclic fatigue process in the fractured rock slope, where many loading cycles
557 induce subcritical fracture propagation until reaching the criticality of the fracture network. Then macroscopic
558 slip is triggered at an apparently random stress perturbation.

559 The hypothesis that rapid strain events often reflect progressive rock mass damage events (e.g., fracture
560 slip) is supported by the observation of abrupt changes in hydromechanical behavior during such events
561 (e.g., step 2 in Fig. 6 and Fig. C 2, Appendix C). This specific event illustrates how the hydromechanically
562 driven diurnal strain cycles can start (FBG-8 and FBG-9) or switch orientation (FBG-7) after a rapid strain
563 event. This change in hydromechanical behavior could be explained by fracture propagation (or slip) induc-
564 ing changes in hydraulic connectivity of the fracture network.

565 3.4.3. Short-term strain signals

566 As introduced above, short-term strain signals at timescales from hours to several days (up to few weeks)
567 often correlate with the pressure head signal in the borehole, which reacts to rainfall and snowmelt infiltra-
568 tion. This is illustrated in Fig. 6, where the strain of FBG-7 clearly follows the pressure head variability in-
569 duced by a rainfall infiltration event (Rec2, panel a, b) or shows good agreement with the winter pressure

570 head in general (panel d, e).

571 Similar to the diurnal strain cycles, we propose that these short-term strain signals originate from hydrome-
572 chanical effects related to pore pressure changes. In contrast to the diurnal cycles that show reversible
573 (elastic) strain, short-term strain signals are often composed of both reversible and irreversible strain com-
574 ponents. A significant rapid strain event that coincided with an extreme rainstorm event in early Oct. 2020
575 (see label b in Fig. 7) was recorded in borehole B2. Although we do not have pore pressure data from
576 borehole B2, we assume a similar pressure increase as measured in B4 during this exceptional event that
577 probably triggered the clearly irreversible strain of some tens to few hundreds of microstrain measured in
578 several shallow FBG sensors of B2. In the other two boreholes, only a minor strain reaction was detected
579 during this specific rainstorm event. We explain this with either higher rock mass quality (B4, cf. section 1.2)
580 or only minor pore pressure reactions to infiltration caused by increased transmissivity (B6, see Fig. C 1).

581 ### 3.4.4. Seasonal transition of the englacial hydrological system

582 Fig. 7 shows the FBG strain data of the ten sensors installed in B2. A comparison of the strain data with
583 water pressures measured in the glacial sinkhole (black line in figure) shows that timing of the switch of the
584 englacial hydrological system coincides with specific strain signals measured in most of the sensors (gray
585 bars in fall 2019 and spring 2020). These signals last for some weeks, often show cyclic behavior, strain
586 magnitudes around 20 με, and mark the start or stop of the diurnal strain cycles that occur only during
587 summer season. The time at which these signals occur differs between years. These distinctive signals are
588 also clearly detectible in spring 2019 and fall 2020. While these signals are clearest in B2, the borehole
589 located most proximal to the glacier margin, they also occur in the other boreholes, but are slightly lower in
590 magnitude in B6 (around 15 με) clearly lower in magnitude in B4 (~ 10 με, see Fig. 6d, step 7) located further
591 away from the glacier margin.

592 We hypothesize that these strain signals are caused by varying glacial loads related to changing water
593 content in the glacier during the seasonal transition phase of the englacial hydrological system. These strain
594 signals cannot be related to direct hydromechanical effects because no such signals occur in the pore pres-
595 sure data of B4 and B6. Based on interpretations of englacial water pressures from many boreholes along
596 the total length of a temperate glacier, Fudge et al. (2005) and Harper et al. (2005) described in detail the

transition phase from summer mode (diurnal pressure fluctuations) to winter mode (steady, high englacial water pressures), and vice versa. Fudge et al. (2005) observed episodic, acyclic water pressure events throughout autumn before values became high and stable. During the spring transition phase, Harper et al. (2005) noted an approximately two weeks long period where both pressure records and glacial sliding velocity demonstrated a high level of activity related to increased meltwater supply and the evolution of the subglacial drainage system.

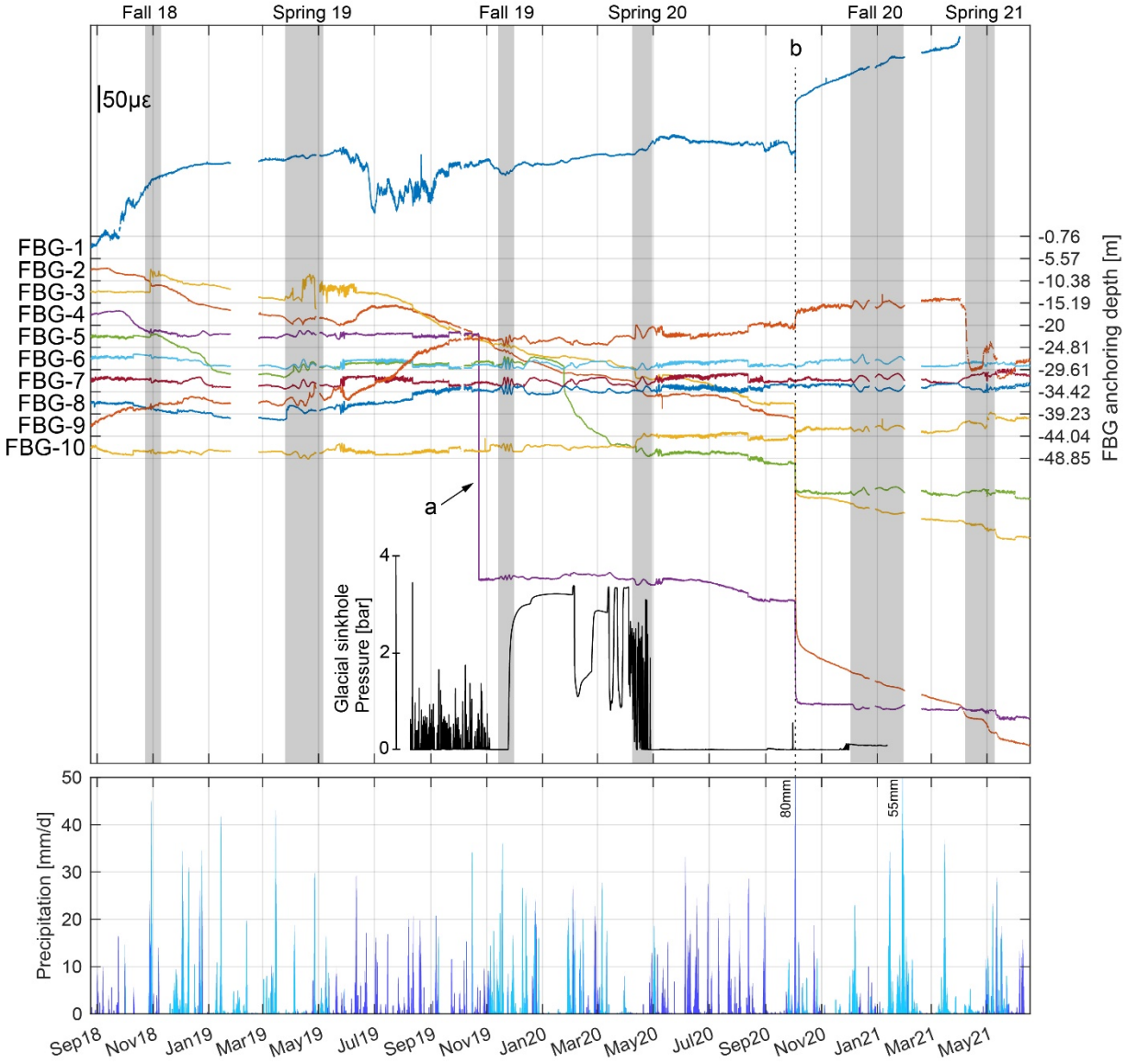

Fig. 7. Temperature corrected FBG strain time series of individual 4.81 m base-length sensors installed in borehole B2 modified of after Hugentobler et al. (2021). The strain data (colored lines) is plotted at the center of the specific depth interval with anchoring depth labeled on the right side. Positive strain equals axial extension and negative strain contraction. The strain scale is provided in the upper left corner in microstrain (µm/m). The black line in the lower center of the upper panel contains pressure time series monitored in the glacial sinkhole for comparison. The gray bars in the upper plot label specific times referred to in the text. Label a indicates a strain step in sensor FBG-4 that was identified as an artifact and therefore is not used for interpretation. Label b indicates an extreme rainstorm event referred to in the text. The lower bar plot shows the cumulative total precipitation data per 24 h from the Bruchji weather station (Valais) located approximately 6 km away from the study site (data provided by MeteoSchweiz). Cyan bars indicate precipitation that probably occurred as snow (i.e., at surface temperatures below 1°C (Jennings et al., 2018)).

3.4.5. Long-term rock slope response to glacier retreat

The comparison of ice levels at the three borehole locations with the vertical strain history between fall 2018 and spring 2021 (Fig. 8) indicates systematic axial shortening (negative strain) following the decreasing glacial ice level. In borehole B2 and B6 the negative strain is detected at shallow sensors, whereas in B4 negative strain is observed also at greater depth. We have to note, that there are also some strain sensors that do not show a negative strain following ice retreat.

Axial shortening measured with the FBG system together with a downslope oriented movement measured in horizontal direction (see inclinometer data in Appendix B, clearly detected in B2 and B6) can originate either from slip along toppling fractures steeply dipping into the slope or sliding fractures dipping in downslope direction. Both frequently occur at our study site (see Fig.4 in Hugentobler et al., 2020). We hypothesize that the observed deformation, that follows the glacial ice level, originates from fracture slip or creep related to the destabilizing effect from unloading by glacial downwasting (i.e., reduced normal load on fractures). Processes potentially driving longer term elastic deformations in deglaciating environments such as rebound from ice unloading or thermoelastic expansion due to ground warming after ice retreat cannot explain the observed negative (contractional) strain. Hydromechanical and thermomechanical fatigue processes may contribute to the observed negative strain trend above ice elevations but are unlikely to cause the systematic strain signals following ice elevation, especially the one observed in B4. This because significant pore pressure magnitudes predominantly occur at deeper borehole locations and thermomechanical

effects are restricted to the shallow thermally active layer (Hugentobler et al., 2021).

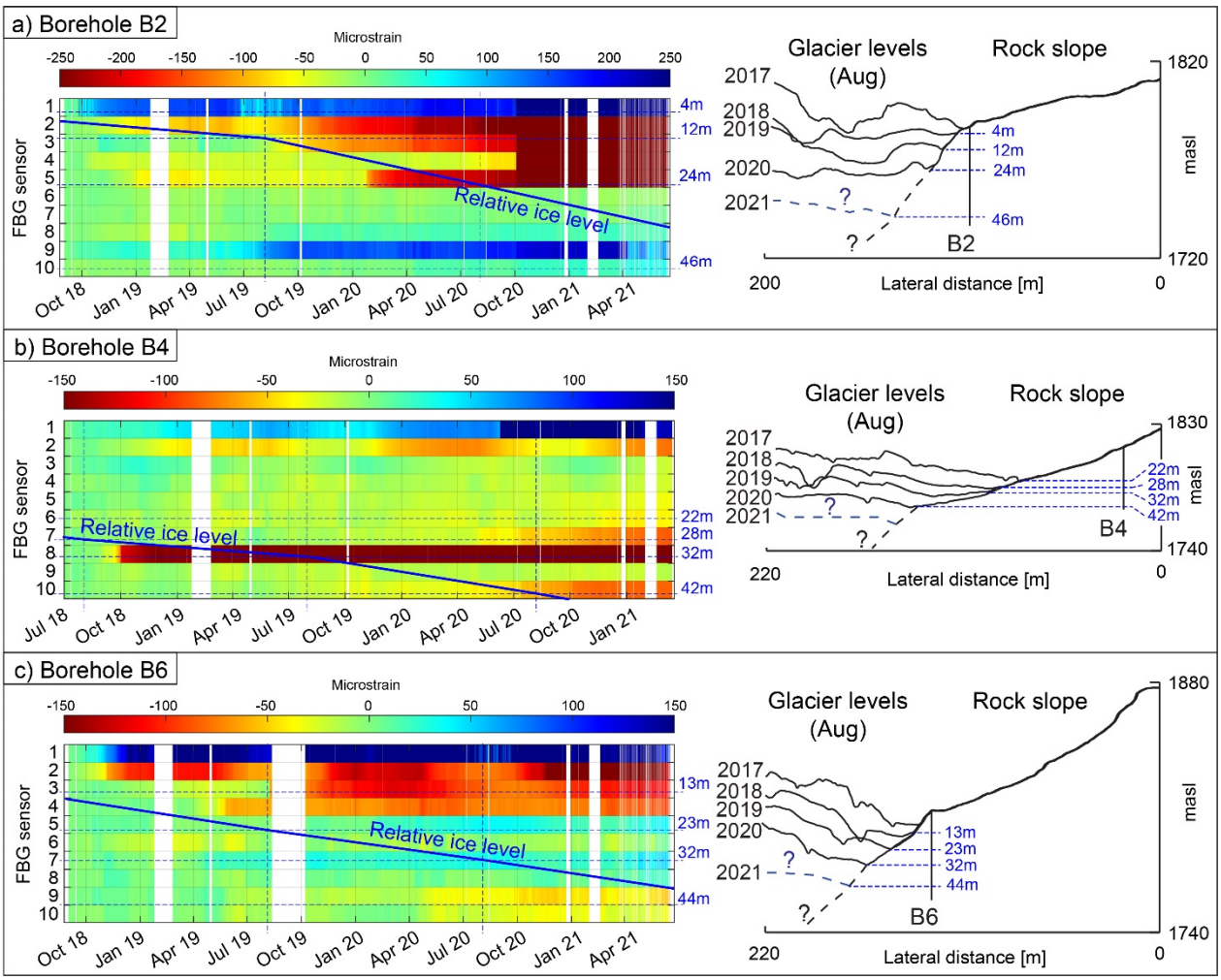

Fig. 8. Color plots show positive (expansion) and negative (contraction) FBG strain measured in the three boreholes. The blue line in the color plots indicate ice elevation at the glacier-slope contact relative to the sensor depth at the specific borehole. These are constructed using the scaled cross-sections to the right of the plots containing yearly high-resolution glacial ice elevation measurements acquired during August (source: Swiss Federal Office of Topography).

3.5. Magnitudes and drivers for irreversible strain

To improve our understanding of irreversible strain magnitudes and mechanisms in our time series we provide a comparison of rapid, continuous, and total irreversible strain at each sensor (Fig. 9a-c) and a time- and depth-integration per borehole location (Fig. 9d-f). Total irreversible strain per sensor is calculated as the difference between the strain recorded at the start and end of our monitoring period. We use only two

full years instead the nearly 3 years of strain data to cancel out annual cyclic thermoelastic driven strain detected in the shallow sensors (Fig. 5, Fig. 7, Fig. C 1 and Hugentobler et al. (2021)). Rapid strain events (i.e., fracture slip) were automatically retrieved from the time series and divided in events with magnitudes smaller and greater 20 με. Continuous strain (i.e., fracture creep) is then calculated by a subtraction of the strain resulting from the summed up rapid events and the total irreversible strain. The provided magnitude of rapid events in Fig. 9a-c reflects the difference between the sum of the positive rapid strain events and the sum of the negative rapid events (illustrated with the error bars in the plot).

Fig. 9a-c emphasizes big difference in activity between the three borehole sites and the depth dependence of the strain signal. In agreement with the inclinometer data (Appendix B), B2 shows the highest activity and B4 and B6 show clearly lower activity. In most sensor intervals of B4 and B6, continuous strain accounts for most of the total irreversible strain and rapid strain events play a minor role (Fig. 9b, c, e, and f). In B2, continuous strain also plays an important role for total irreversible strain, but rapid strain events account for more than 50 % of the total irreversible strain (Fig. 9a and d). The dominance of rapid events for the total irreversible strain is related to a single extreme rainstorm event in October 2020 (label b in Fig. 7) that resulted in all rapid events > 20 με (black bar) in this borehole. Rapid events < 20 με related to changes in mechanical glacial loads do not show an increased effect in this borehole compared to the other two.

We attribute most of the continuous irreversible strain in all the boreholes to ice unloading effects (cf. section 3.4.5), and a minor portion of the continuous irreversible strain to accumulate from not fully reversible short-term hydromechanical driven strain events correlating with pressure head fluctuations (section 3.4.3). Although rapid strain events related to changes in mechanical glacial loads (events < 20 με) are numerous, account for significant strain in extension and contraction direction (error bars in Fig. 9), these events do not dominate the total irreversible strain of the two-year sampling period. In B6, the sum of these rapid events shows strain in extension direction, which is the opposite direction of the total irreversible strain. The rapid strain events > 20 με that are related to the single extreme rainstorm event strongly affected the total irreversible strain of the two years in the shallow 20 m of B2. According to borehole televiewer images, the shallow 25 m of this borehole shows an increased fracturing compared to greater depth or the B4 site and contains many open or filled joints (Hugentobler et al., 2020).

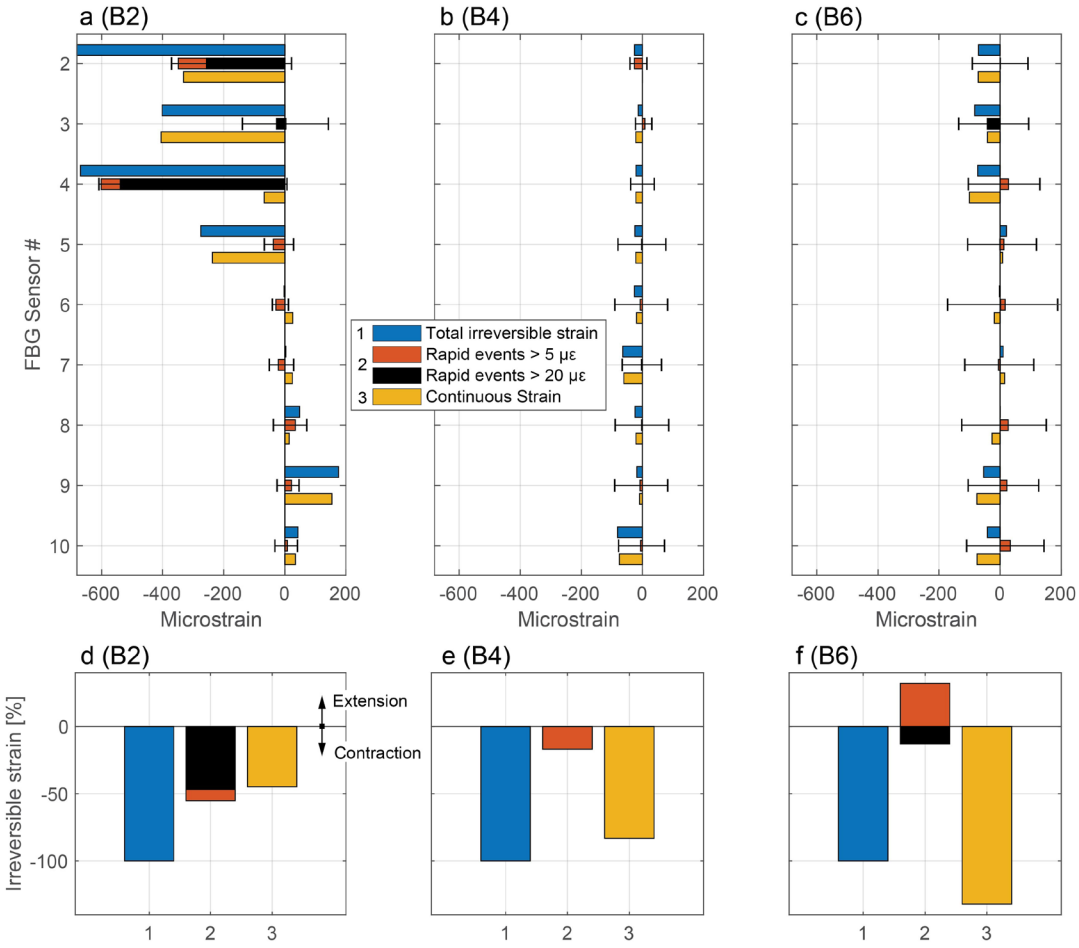

Fig. 9. Visualization of irreversible FBG strain per sensor between Nov. 2018 and Nov. 2020 (a-c). Error bars for the rapid strain events shows the sum of the positive (extension) and the sum of the negative (contraction) rapid strain events. Panels d-f show the sum of total irreversible strain, rapid strain events, and continuous strain of all sensors in each borehole in %. The uppermost FBG sensors of all boreholes are not shown and used for the analysis because they contain uncomplete data recordings because of malfunctioning reflected light peak detections.

4. Discussion

4.1. Transient boundary conditions at a retreating glacier margin

In this section, we summarize our understanding of thermal, hydraulic and mechanical boundary conditions that affect a rock slope subject to glacial ice retreat at timescales of our monitoring campaign (i.e., from hours to three years, Fig. 10). Such data supported knowledge is unique and crucial for understanding of

683 the main drivers for deformation and progressive damage in paraglacial rock slopes.

684 Thermal boundary conditions in our monitored rock slope were investigated in detail in Hugentobler et al.
685 (2021), considering changes on timescales ranging from days to decades. Bedrock below temperate glacial
686 ice stays at a relatively constant temperature of around 0 °C. Above ice elevations, diurnal temperature
687 cycles affect the uppermost decimeters of the rock surface and occur only during the snow free summer
688 season (Fig. 10a). Seasonal temperature cycles penetrate down to a depth of 15 to 20 m (Fig. 10b) with
689 temperature amplitudes that exponentially decay with depth (Hugentobler et al., 2021). On decadal time-
690 scales, glacial retreat leads to bedrock exposure and changes the thermal boundary to a new mean annual
691 ground temperature that penetrates the subsurface down to greater depth at a pace controlled by the ther-
692 mal diffusivity of the rock mass (i.e., around 150 m in a century) (Hugentobler et al., 2021) (Fig. 10c).

693 Changes in hydraulic boundary conditions in a glacial adjacent rock slope that occur at timescales from
694 hours to decades are illustrated in Fig. 10d-f. At the timescale of days, diurnal meltwater cycles and rainfall
695 infiltration into the glacier during summertime cause strong pressure fluctuation in the subglacial drainage
696 channel (with magnitudes from nearly ice overburden down atmospheric values) that diffuse into the adja-
697 cent rock aquifer (Fig. 10d). We show that the pressure diffusion from the subglacial meltwater channel,
698 through the fractured bedrock below the glacier ice, to the ice-free bedrock slope occurs under predomi-
699 nantly confined conditions (Section 3.3.2). In the adjacent ice-free bedrock, rainfall infiltration causes varia-
700 tions in the phreatic groundwater table of the slope (Fig. 6). On the seasonal timescale (Fig. 10e), glacial
701 hydraulic boundary conditions vary with high, relatively constant englacial water levels during wintertime
702 and lower mean englacial water levels during summertime (Fig. 3). Above ice elevations, snowmelt infiltra-
703 tion during springtime causes yearly maximum phreatic groundwater tables and a general recession over
704 the rest of the year, that is interrupted by summertime rainfall infiltrations (Fig. 2). The seasonality in hy-
705 draulic head levels of both the glacier and the rock slope controls the interaction of the two systems. Hence,
706 we propose that glacial hydraulic BCs act similar as a river with losing condition during wintertime (i.e.,
707 glacier lose water to groundwater) and gaining condition during summertime (i.e., englacial water gains
708 water from the adjacent groundwater system). On timescales of decades (Fig. 10f), phreatic groundwater
709 levels in the rock slope are often assumed to be linked to the ice elevation of temperate glaciers (e.g.,

Grämiger et al., 2020; McColl et al., 2010). According to our data (Fig. 2), this head boundary effect of the glacier is mainly effective during wintertime when it controls the minimum groundwater level in the slope (i.e., losing condition). Therefore, the effect of this boundary condition is assumed to be more important for high glacier levels above the valley bottom.

Our results show that the variations in mechanical boundary conditions (or loads) caused by a temperate valley glacier on the adjacent rock slope are more complex than had been previously described. Our observed rapid bedrock strain signals coinciding with some of the extreme englacial water level states, summarized in Section 3.4.2, are likely caused by rapid changes in the mechanical load of the glacier with an empty or water filled englacial drainage system (Fig. 10g). Similarly, but at seasonal timescales, the spring and fall transition time of the englacial hydrological system from low, dynamic summertime water pressures to steady, high wintertime pressures coincides with characteristic strain reactions in our bedrock slope (see gray bars in Fig. 7). On the timescales of decades, changing glacial loads from ice downwasting cause irreversible shortening deformations in our monitored rock slope (Fig. 8).

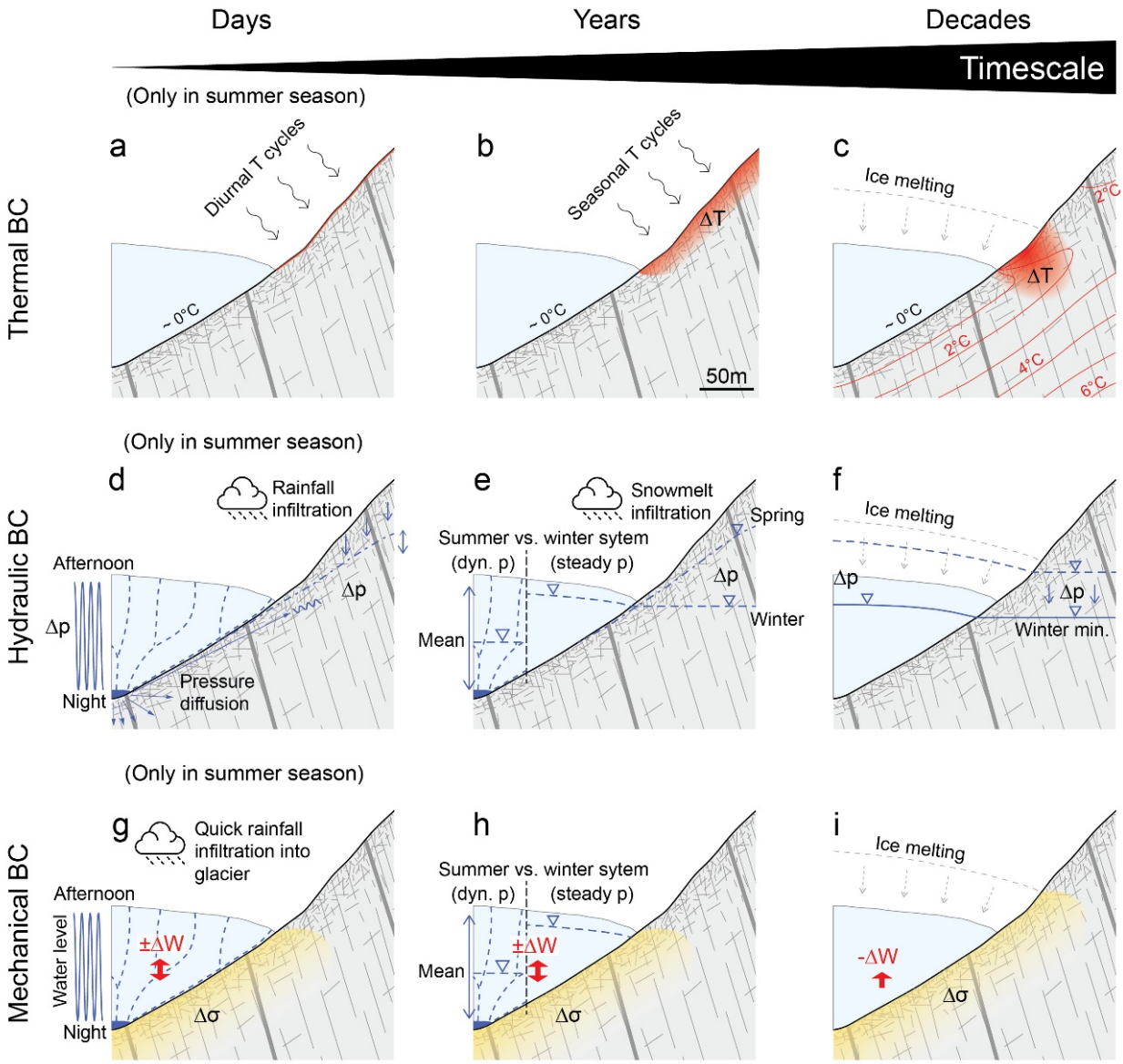

724 *Fig. 10. Visualization of thermal, hydraulic, and mechanical loads that affect glacial adjacent rock slopes and potentially*
725 *drive deformation and progressive rock mass damage at timescales from hours to decades. Thermal boundary condi-*
726 *tions (BC) are in detail investigated in Hugentobler et al. (2021).*

727 4.2. Rock slope reactions to changing boundary conditions

728 All the above changes in boundary conditions cause changes in loading conditions of the glacial adjacent
729 rock slope and lead to reversible and irreversible slope deformations at different magnitudes and timescales.
730 Table 1 compiles our recorded strain signals from section 3 and Hugentobler et al. (2021). This table com-
731 prises ranges of total (reversible and irreversible) strain magnitudes that are caused by the specific load

732 change and information about the strain characteristics. The data is used to discuss the relative importance
733 of the different drivers for rock slope deformation and progressive rock mass damage.

734 *Table 1. Summary of observed total (reversible and irreversible) strain magnitudes related to thermo-hydro-mechani-*
735 *cal loads described above.*

BC	Timescale	Panel Fig. 10	Total strain magnitudes	Strain characteristics
Thermal	Years	b	60 με (~4m) – 5 με (~20m)[1]	Mainly reversible, continuous
Hydraulic	Days (summer)	d	5 με	Reversible, continuous
Hydraulic	Years	e	20 με[2]	Partly reversible, continuous
Mechanical	Days (summer)	g	5 – 10 με (max. ~ 20 με)	Often irreversible, rapid
Mechanical	Years	h	20 με	Mainly reversible, continuous
Mechanical	Decades	i	Between 0 and ~ 100 με/a	Irreversible, continuous

1: Hugentobler et al. (2021); 2: without considering the extreme rainstorm of Oct. 2020

736

737 Our detailed analysis of subsurface hydromechanical (present study) and thermomechanical (Hugentobler
738 et al., 2021) responses supports the identification of potential drivers for irreversible deformation down to a
739 depth of around 50 m and at timescales from hours to a few years. In boreholes B4 and B6, the highest
740 irreversible strains, which we relate to progressive rock mass damage, are assumed to be driven by me-
741 chanical unloading due to long-term glacial ice downwasting. In borehole B2, an extreme rainfall event trig-
742 gered rapid irreversible deformation (presumably by pore pressure increase from infiltration) that slightly
743 exceeded the magnitude of the two-year continuous deformation mainly attributed to ice unloading (Fig. 8).
744 Additionally, hydromechanical effects related to snowmelt and summertime rainfall infiltration and changes
745 in mechanical loading due some extreme stages of englacial water levels were identified to contribute to the
746 irreversible deformation.

747 Our monitoring data support the hypothesis that retreating temperate valley glaciers cause significant
748 thermo-hydro-mechanical perturbations of the boundary conditions affecting adjacent rock slopes and con-
749 tributing to progressive rock mass weakening (Ballantyne et al., 2014; Grämiger et al., 2020; McColl, 2012;
750 McColl and Draebing, 2019; Prager et al., 2008; Riva et al., 2017). Few previous numerical studies that
751 investigated paraglacial rock slope evolutions over the timescales of glacial cycles have chosen simplified,
752 but adequate, assumptions for thermal and hydraulic boundary condition including annual pore pressure

753 and temperature cycles (Grämiger et al., 2018; Grämiger et al., 2020). However, diurnal cyclic glacial loads
754 during the summer season related to fluctuating water levels in the glacier have never been considered in
755 such studies. Our in-situ data show that these effects also promote progressive rock mass damage, proba-
756 bly similar to hydromechanical effects (section 3.5). Additionally, we show how a single extreme rainstorm
757 event triggers hydromechanical damage exceeding the levels of two years exposition to all the other drivers
758 for progressive rock mass damage in this environment. This emphasizes the importance to consider extreme
759 weather events as drivers for rock mass damage over longer periods of time.

760 In contrary to the numerical study of Grämiger et al. (2020), who found that hydro-mechanical effects ac-
761 companying glacial ice fluctuations are more efficient in generating rock mass damage than only changes
762 in mechanical ice loads, we postulate that the largest observed irreversible strain magnitudes are related to
763 unloading from ice retreat. However, the relative importance of the different drivers is probably not constant
764 at the slope scale. Processes directly related to transient glacial boundary conditions (e.g., pore pressure
765 diffusion effects from transient englacial water pressures, stress transfer from changing glacial loads, sur-
766 face temperature changes related to newly uncovered rock surface) cause the strongest stress perturba-
767 tions in the rock slope below ice levels or close to the glacier margin, i.e., where our boreholes are located.
768 Longer-term delayed subsurface temperature changes due to deglaciation impact the rock slope far away
769 from the ice margin (Hugentobler et al., 2021). Conversely, hydromechanical effects related to pore pressure
770 fluctuations above ice levels with amplitudes mainly controlled by the ratio of infiltration and hydraulic diffu-
771 sivity as well as thermomechanical effects related to annual temperature cycles impact the whole rock slope
772 above ice elevations.

773 In summary, our in-situ data shows that reversible and irreversible deformation is a result of stress changes
774 by superimposed thermo-hydro-mechanical processes that may act at similar orders of magnitude. The
775 relative importance of the different drivers for progressive rock mass damage strongly depends on the slope
776 location relative to the glacier margin, mechanical and hydraulic rock mass properties (controlling local
777 stress magnitudes and stress transfer), and depth (controlling thermo-mechanical stress magnitudes, cf.
778 Hugentobler et al. (2021)). Although, no relationship between strain events in the boreholes and nearby

earthquakes could be observed during our monitoring period (cf. Hugentobler et al., 2021), earthquake activity potentially increased by glacio-isostatic adjustment (Ballantyne et al., 2014; Cossart et al., 2014) could also contribute to progressive rock mass damage on the long-term.

5. Conclusion

This study is based on detailed analysis of subsurface borehole monitoring data in a rock slope affected by rapid glacial ice retreat and englacial water level measurements from a nearby glacial sinkhole. This data set allows us to constrain the previously hypothesized transient thermal, hydraulic and mechanical boundary conditions that act at different timescales and induce small rock slope deformations in such a deglaciating environment. This knowledge is key for the understanding of the main processes contributing to progressive rock mass weakening that potentially leads to the formation of paraglacial rock slope instabilities over long time scales. The main findings of this study can be summarized as follows:

- Pore pressures in our rock slope are affected by both direct snowmelt and rainfall infiltration and hydraulic boundary conditions caused by the adjacent temperate glacier. Similar to non-glaciated Alpine rock slopes phreatic groundwater levels in the slope show an annual cyclicity with maximum level after snowmelt infiltration in spring followed by a recession over the rest of the year that is interrupted by infiltration from significant rainfall or snowmelt events in summer and fall. Englacial water levels of temperate valley glaciers affect pore pressures in adjacent rock slopes on (1) diurnal timescales during summertime with pressure signals diffusing into the slope, (2) on annual timescales as a constant head boundary due to high constant water levels that define a minimum elevation of the phreatic slope water table, and (3) on decadal timescales with minimum wintertime phreatic slope water tables following the ice elevations.

- Rapid- and short-term total (i.e., reversible and irreversible) deformation at timescales from hours to weeks in our monitored rock slope can be attributed to (1) poroelastic responses of diurnal fluctuations in pore pressures caused by englacial water pressure fluctuations diffusing into the slope, (2) stress transfer from changing mechanical glacier load related the diurnal englacial water level changes, and (3) hydromechanical effects related to pore pressure fluctuations from snowmelt and rainfall infiltration events.

- Longer-term total (i.e., reversible and irreversible) deformation at timescales from month to years are related to (1) thermomechanical effects from annual temperature cycles penetrating the shallow subsurface, (2) hydromechanical effects from seasonal pore pressure fluctuations driven by the main snowmelt in springtime and an overall recession over the rest of the year, and (3) mechanical unloading related to glacial ice downwasting.

- Irreversible deformation, which we relate to progressive rock mass damage, showed to be mainly driven by longer-term stress changes related to mechanical unloading from glacial ice downwasting, and shorter-term stress changes from diurnal mechanical loading cycles related to englacial water level fluctuations and hydromechanical effects related to pore pressure variations from snowmelt and rainfall infiltration.

Acknowledgements

This project was funded by the Swiss National Science Foundation (project 172492). We want to thank Danial Farinotti from the Laboratory of Hydraulic, Hydrology and Glaciology (VAW) at ETH Zurich for providing equipment and know-how for ice-drilling and installing sensors and data loggers on the Great Aletsch Glacier. Also, we thank the many field helpers for their support during several maintenance visits that enabled the nearly continuous monitoring of subsurface data under harsh Alpine conditions. Special thanks go to Nicolas Oestreicher for joining many of our glacier expeditions. We also want to thank Valentin Gischig for supporting the planning of the project and Reto Seifert for his technical expertise and support on all the remote monitoring systems. Further, we acknowledge Aslak Grinsted for providing the tidal fitting toolbox used in this study. Data is accessible under: https://doi.org/10.3929/ethz-b-000505871.

6. Appendix A: Pore pressure signal deconvolution and effects of earth tides

As visible in Fig. 3 during wintertime, both boreholes additionally show signals at frequencies at around 1 cpd and greater. These signals occur at pressure head amplitudes of ~ 0.02 m which is slightly lower than the diurnal summertime fluctuations in B6 but an order of magnitude lower than the daily summertime cycles in B4. A signal deconvolution into the frequency domain (using fft) allows a detailed analysis of the signals

contained in the data. Because the signals strongly differ between the summer and winter season, we provide the signal analysis in the frequency domain for both seasons (Fig. A 1). Hence, amplitude spectra in the frequency band between around 1 to 2 cycles per day are calculated for atmospheric pressure, earth tides in the study area computed with Tsoft (Van Camp and Vauterin, 2005), and pore pressures in boreholes B4 and B6. The results in Fig. A 1 show that during winter season peaks in the amplitude spectra of the B4 pore pressure signal show similar frequencies as the computed earth tides. B6 pore pressure signal during wintertime shows the same frequencies as the atmospheric pressure. During summer season, the amplitude spectra of the pore pressures in the two boreholes show a clearly dominating peak at the frequency of 1 cpd. These peaks show an amplitude increase of one order of magnitude in B4 and about 5 times in B6 compared to wintertime. Although a 1 cpd frequency peak also occurs in the computed earth tides and the atmospheric pressure, these signals cannot explain the observed amplitude increase in the pore pressures during summer season because they stay more or less constant over the whole year. Hence, the 1 cpd peak observed in the pore pressure readings of the two boreholes must be explained by a different process.

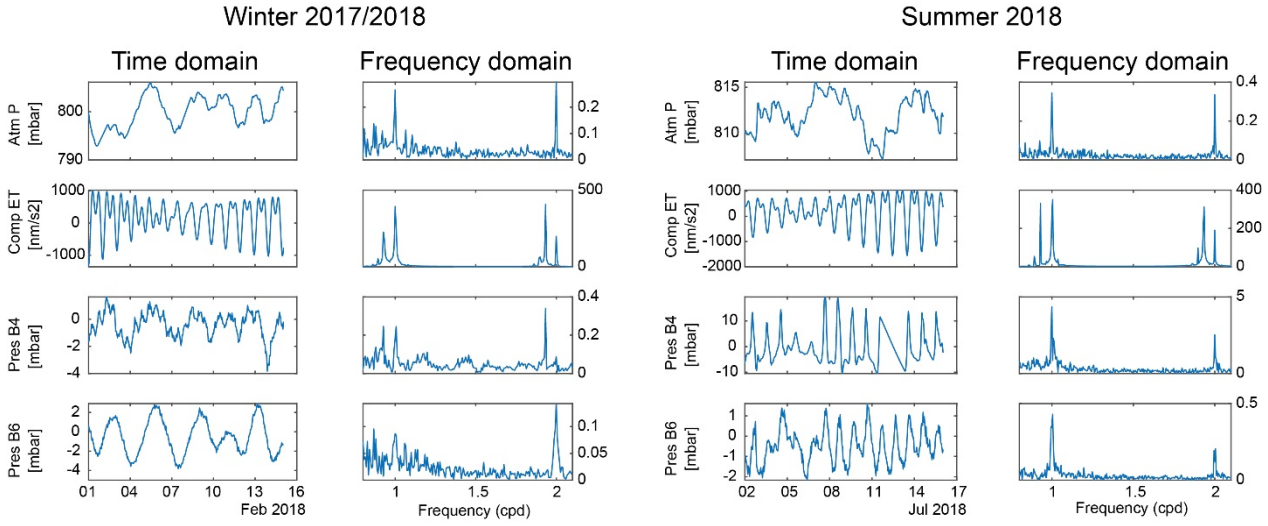

Fig. A 1. Comparison of atmospheric pressure (Atm P) measured in the study area, computed earth tides (Comp ET) for the study area, and pore pressure in borehole B4 (Pres B4) and B6 (Pres B6) in the time and frequency domain during winter and summer season.

As introduced above, the existence of main tidal components (e.g., O_1, K_1, M_2, and S_2) and its relative

amplitudes compared to atmospheric tides (e.g., S1 and S2) contained in pore pressure measurements allow to investigate the degree of confinements of aquifers. A description of the origin of the most important Earth and atmospheric tidal components can be found in table 1 of McMillan et al. (2019). Fitted tidal components on the undisturbed sections of the high pass filtered wintertime pore pressure data in borehole B4 and B6 are provided in Fig. A 2c-f in the time and frequency domain. For comparison the computed Earth tide signal for the study area is provided in Fig. A 2a, b. The fitted tidal components for B4 data can account for around 50 % of the signals' variance during wintertime and for the B6 data for about 30 %.

According to Rahi and Halihan (2013) an aquifer behaves semiconfined when the S2 component dominates but M2 is still present. If M2 is dominating, the aquifer behaves confined and where M2 is not present the aquifer is unconfined (Bredehoeft, 1967; McMillan et al., 2019; Rahi and Halihan, 2013). According to this classification the aquifer around B4 behaves confined and at B6 semiconfined.

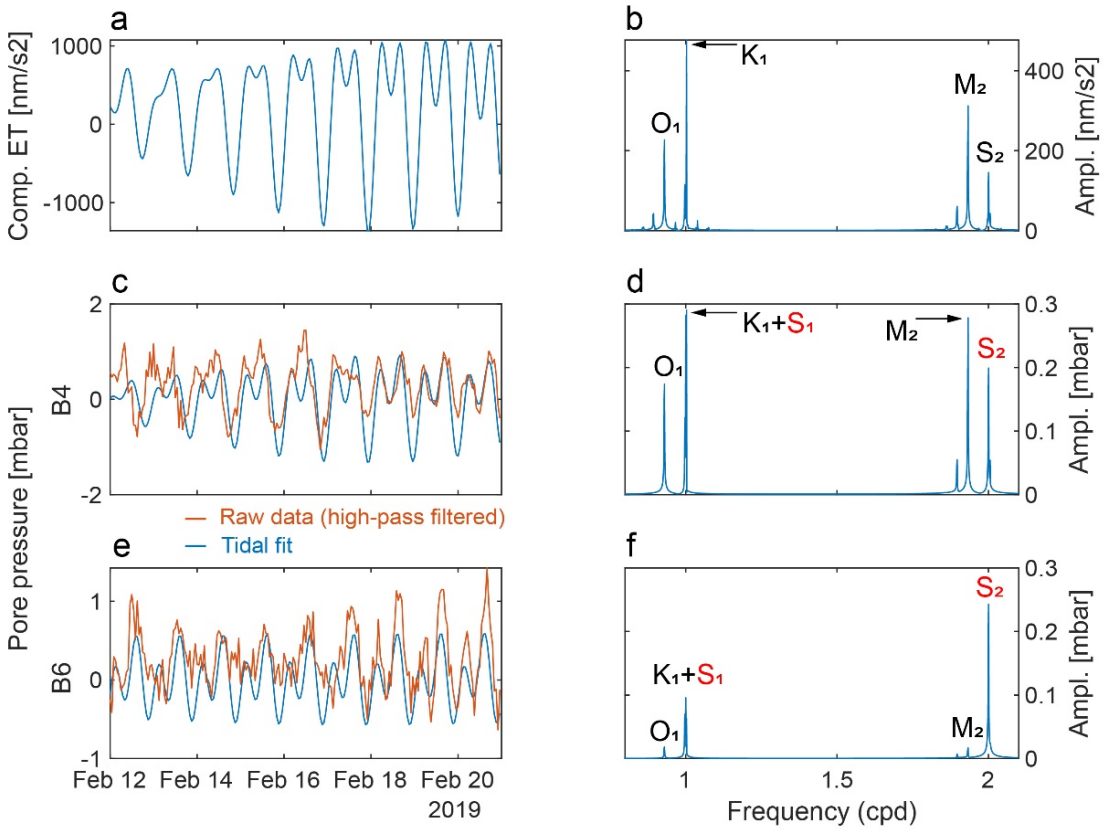

Fig. A 2. Comparison of computed Earth tides (Comp ET) for the study area and fitted tidal components to the high pass filtered pore pressure data of B4 and B6 visualized in the time and frequency domain. In panels b, d, and f the main tidal components (O_1, K_1, M_2, and S_2) and atmospheric tides (S_1 and S_2) are indicated.

7. Appendix B: Horizontal deformation

The cumulative horizontal deformation in the B2 and B6 shows a clear overall downslope movement indicated with the black arrows in the map view illustration (Fig. B 1a-d). At B4 location the overall movement direction is slope parallel. The highest magnitude of about 17 mm in approximately two years is observed in borehole B2 and clearly lower values are measured in B4 and B6. In B2 the majority of the deformation occurs in the uppermost 20 m but minor deformation is also observed in greater depth (Fig. B 1e). In B4 deformation is distributed over the whole length of the borehole but shows early activity in greater depth (Fig. B 1f). Deformation in B6 predominantly occurs at few discrete locations (Fig. B 1g). Superimposed to these irreversible trends, annual reversible cyclic deformation is also observed (e.g., in B4 in downslope

direction, Fig. B 1b).

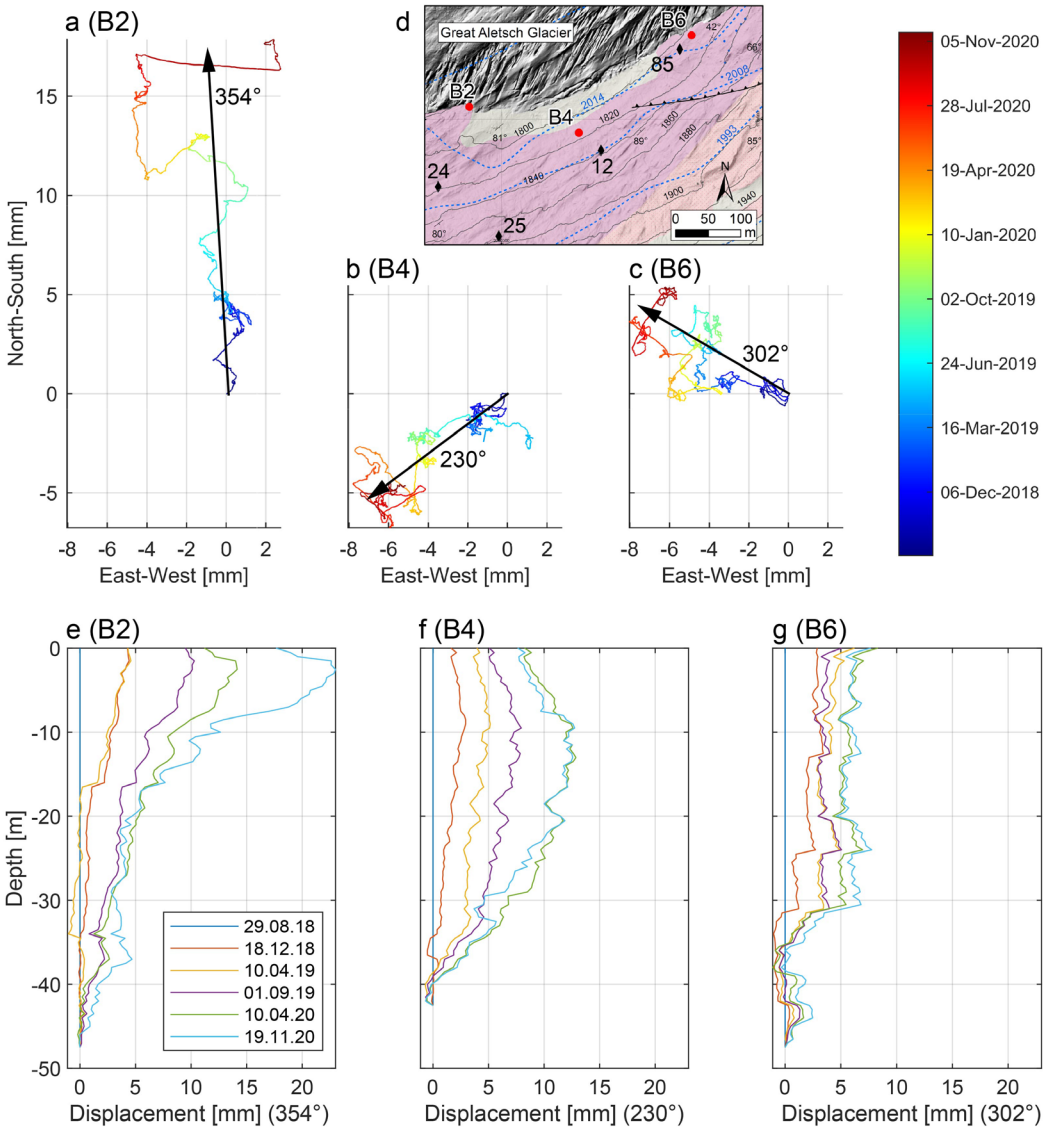

Fig. B 1. a, b, c: Map view illustrations of cumulative horizontal deformation over time of boreholes B2, B4, and B6 measured with the SAA in-place inclinometer system adapted from Hugentobler et al. (2021). The black arrows indicate the mean movement direction. d: Map view of the three borehole locations. e, f, g: Cumulative displacements of each segment form the borehole end up to the surface in direction of the main movement.

Appendix C: FBG strain time series

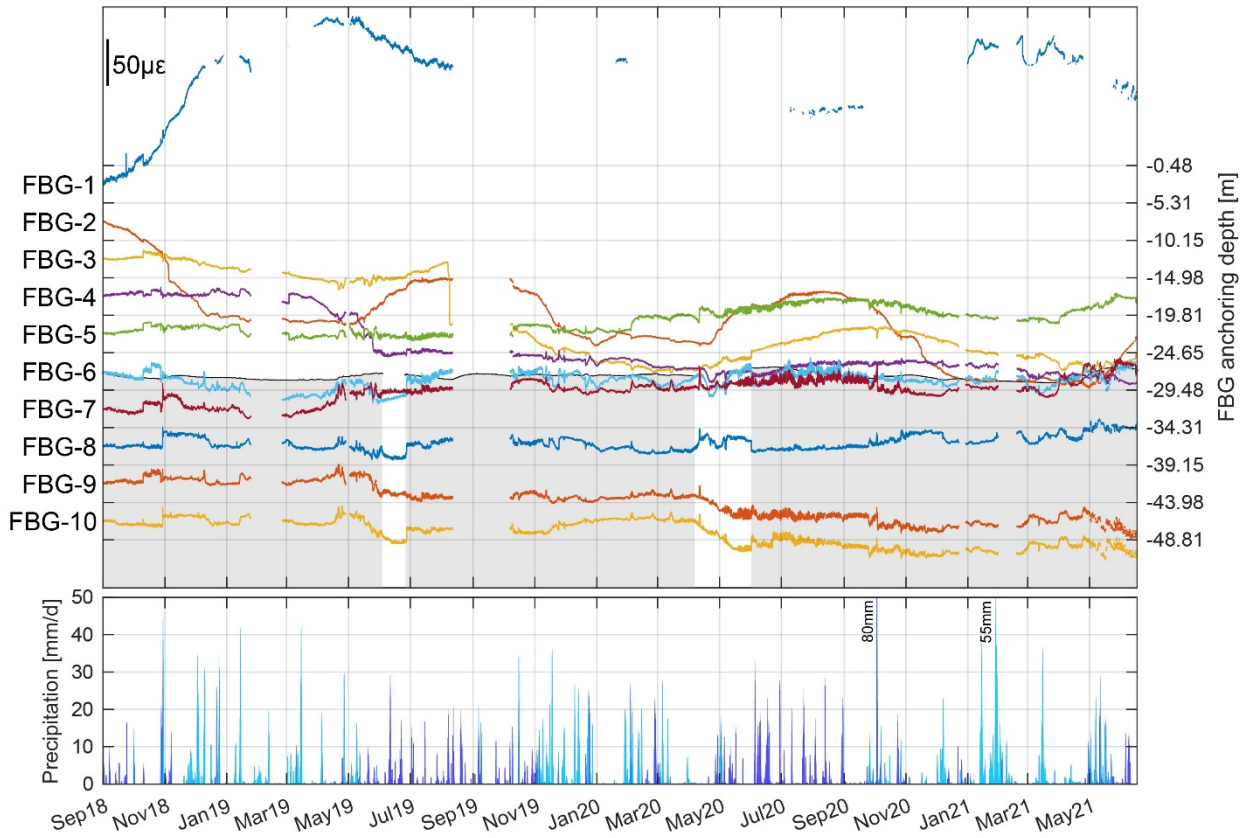

Fig. C 1. Temperature corrected FBG strain time series of individual 4.83 m base-length sensors installed in borehole B6 visualized of after Hugentobler et al. (2021) with added data form winter/spring 2021. The strain data (colored lines) is plotted at the center of the specific depth interval with anchoring depth labeled on the right side. Positive strain equals axial extension and negative strain contraction. The strain scale is provided in the upper left corner in microstrain (μm/m). The elevation of the pressure head is provided as a gray area in the background. The lower bar plot shows the cumulative total precipitation data per 24 h from the Bruchji weather station (Valais) located approximately 6 km away from the study site (data provided by MeteoSchweiz). Cyan bars indicate precipitation that probably occurred as snow (i.e., at surface temperatures below 1°C (Jennings et al., 2018)).

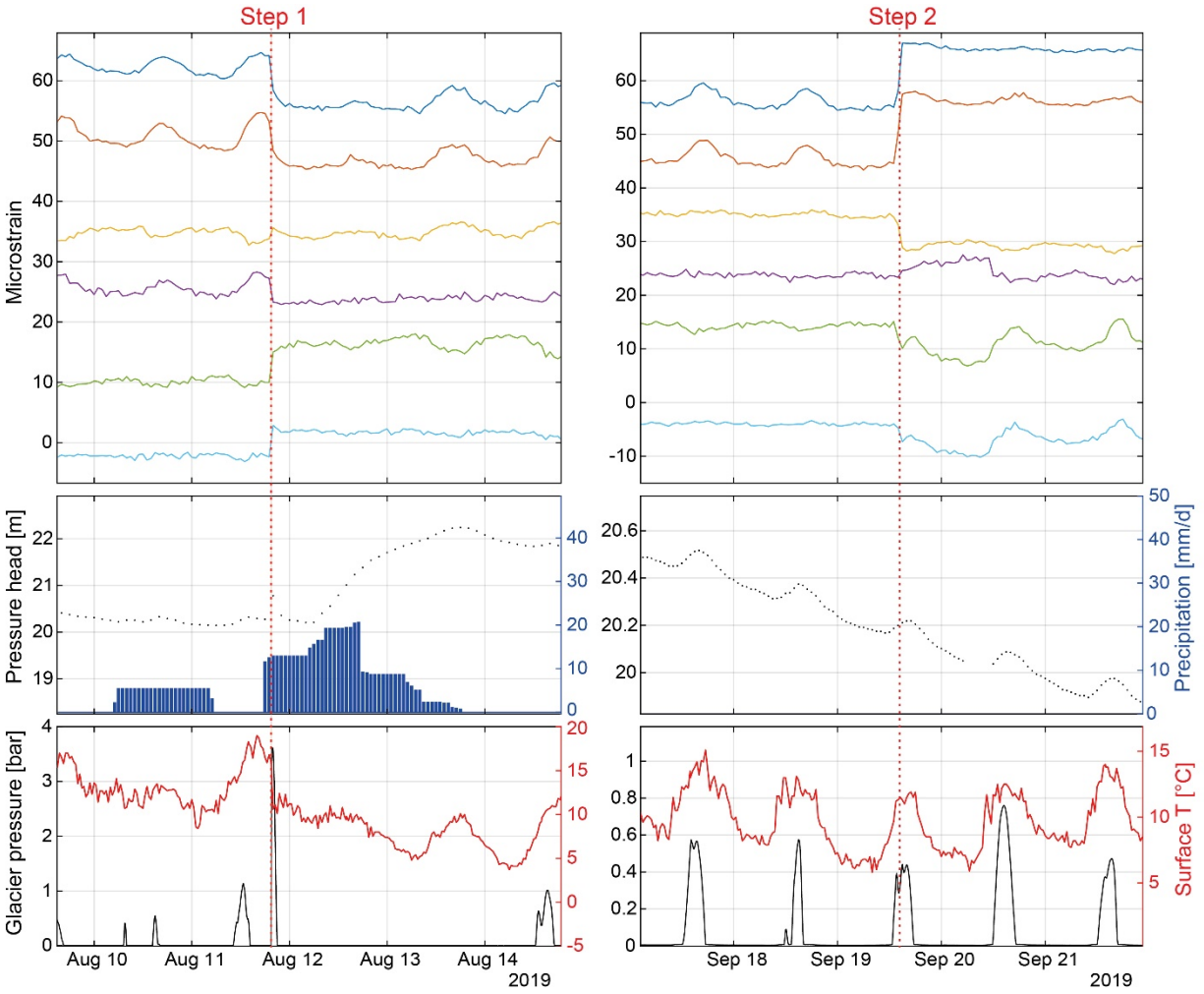

Fig. C 2. First row plots: Zoom on rapid strain events (Step 1 and 2) illustrated in Fig. 6. FBG strain data of the lower six sensors of B4 (FBG-5 to FBG-10) is plotted with 10 με offset for better visualization. Second row plots: Pressure head measured in borehole B4 at 43.75 m depth and Cumulative total precipitation data (per 24 h) provided by MeteoSchweiz from the weather station "Bruchji" (Valais). Third row plots: Pressure measured in the glacial sinkhole at approximately 40 m depth and surface temperature measured at the study site.

References

Achtziger-Zupančič, P., Loew, S., and Mariéthoz, G., 2017, A new global database to improve predictions of permeability distribution in crystalline rocks at site scale: Journal of Geophysical Research: Solid Earth, v. 122, no. 5, p. 3513-3539.

Acworth, R. I., Halloran, L. J. S., Rau, G. C., Cuthbert, M. O., and Bernardi, T. L., 2016, An objective frequency domain method for quantifying confined aquifer compressible storage using Earth and atmospheric tides: Geophysical Research Letters, v. 43, no. 22, p. 11,671-611,678.

Ballantyne, C. K., Sandeman, G. F., Stone, J. O., and Wilson, P., 2014, Rock-slope failure following Late Pleistocene deglaciation on tectonically stable mountainous terrain: Quaternary Science Reviews, v. 86, p. 144-157.

Barker, J. A., 1988, A generalized radial flow model for hydraulic tests in fractured rock: Water Resources Research, v. 24, no. 10, p. 1796-1804.

Baroni, C., Martino, S., Salvatore, M. C., Mugnozza, G. S., and Schiliro, L., 2014, Thermomechanical stress-strain numerical modelling of deglaciation since the Last Glacial Maximum in the Adamello Group (Rhaetian Alps, Italy): Geomorphology, v. 226, p. 278-299.

Barrett, A. P., and Collins, D. N., 1997, Interaction between water pressure in the basal drainage system and discharge from an Alpine glacier before and during a rainfall-induced subglacial hydrological event: Annals of Glaciology, v. 24, p. 288-292.

Bonzanigo, L., Eberhardt, E., and Loew, S., 2007, Long-term investigation of a deep-seated creeping landslide in crystalline rock. Part I. Geological and hydromechanical factors controlling the Campo Vallemaggia landslide: Canadian Geotechnical Journal, v. 44, no. 10, p. 1157-1180.

Brain, M. J., Rosser, N. J., Norman, E. C., and Petley, D. N., 2014, Are microseismic ground displacements a significant geomorphic agent?: Geomorphology, v. 207, p. 161-173.

Bredehoeft, J. D., 1967, Response of well-aquifer systems to Earth tides: Journal of Geophysical Research (1896-1977), v. 72, no. 12, p. 3075-3087.

Chapman, S., and Westfold, K. C., 1956, A comparison of the annual mean solar and lunar atmospheric tides in barometric pressure, as regards their worldwide distribution of amplitude and phase: Journal of Atmospheric and Terrestrial Physics, v. 8, no. 1, p. 1-23.

Cody, E., Draebing, D., McColl, S., Cook, S., and Brideau, M.-A., 2020, Geomorphology and geological controls of an active paraglacial rockslide in the New Zealand Southern Alps: Landslides, v. 17, no. 4, p. 755-776.

Cossart, E., Mercier, D., Decaulne, A., Feuillet, T., Jónsson, H. P., and Sæmundsson, Þ., 2014, Impacts of post-glacial rebound on landslide spatial distribution at a regional scale in northern Iceland (Skagafjörður): Earth Surface Processes and Landforms, v. 39, no. 3, p. 336-350.

de Palézieux, L., and Loew, S., 2019, Long-term transient groundwater pressure and deep infiltration in Alpine mountain slopes (Poschiavo Valley, Switzerland): Hydrogeology Journal.

Eberhardt, E., 2008, Twenty-ninth Canadian Geotechnical Colloquium: The role of advanced numerical methods and geotechnical field measurements in understanding complex deep-seated rock slope failure mechanisms: Canadian Geotechnical Journal, v. 45, no. 4, p. 484-510.

Elkhoury, J. E., Brodsky, E. E., and Agnew, D. C., 2006, Seismic waves increase permeability: Nature, v. 441, no. 7097, p. 1135-1138.

949 Fan, Y., Clark, M., Lawrence, D. M., Swenson, S., Band, L. E., Brantley, S. L., Brooks, P. D.,
950 Dietrich, W. E., Flores, A., Grant, G., Kirchner, J. W., Mackay, D. S., McDonnell, J. J., Milly,
951 P. C. D., Sullivan, P. L., Tague, C., Ajami, H., Chaney, N., Hartmann, A., Hazenberg, P.,
952 McNamara, J., Pelletier, J., Perket, J., Rouholahnejad-Freund, E., Wagener, T., Zeng, X.,
953 Beighley, E., Buzan, J., Huang, M., Livneh, B., Mohanty, B. P., Nijssen, B., Safeeq, M.,
954 Shen, C., van Verseveld, W., Volk, J., and Yamazaki, D., 2019, Hillslope Hydrology in
955 Global Change Research and Earth System Modeling: Water Resources Research, v. 55,
956 no. 2, p. 1737-1772.
957 Fudge, T. J., Harper, J. T., Humphrey, N. F., and Pfeffer, W. T., 2005, Diurnal water-pressure
958 fluctuations: timing and pattern of termination below Bench Glacier, Alaska, USA: Annals
959 of Glaciology, Vol 40, 2005, v. 40, p. 102-106.
960 Gischig, V., Preisig, G., and Eberhardt, E., 2016, Numerical Investigation of Seismically Induced
961 Rock Mass Fatigue as a Mechanism Contributing to the Progressive Failure of Deep-
962 Seated Landslides: Rock Mechanics and Rock Engineering, v. 49, no. 6, p. 2457-2478.
963 Gischig, V. S., Moore, J. R., Evans, K. F., Amann, F., and Loew, S., 2011a, Thermomechanical
964 forcing of deep rock slope deformation: 1. Conceptual study of a simplified slope: Journal
965 of Geophysical Research-Earth Surface, v. 116.
966 -, 2011b, Thermomechanical forcing of deep rock slope deformation: 2. The Randa rock slope
967 instability: Journal of Geophysical Research-Earth Surface, v. 116.
968 GLAMOS, 1881-2019, The Swiss Glaciers 1880-2016/17, Glaciological Reports No 1-138,
969 Yearbooks of the Cryospheric Commission of the Swiss Academy of Sciences (SCNAT),
970 published since 1964 by VAW / ETH Zurich.
971 Gleeson, T., and Manning, A. H., 2008, Regional groundwater flow in mountainous terrain: Three-
972 dimensional simulations of topographic and hydrogeologic controls: Water Resources
973 Research, v. 44, no. 10.
974 Glueer, F., Loew, S., and Manconi, A., 2020, Paraglacial history and structure of the Moosfluh
975 Landslide (1850–2016), Switzerland: Geomorphology, v. 355, p. 106677.
976 Glueer, F., Loew, S., Manconi, A., and Aaron, J., 2019, From toppling to sliding: progressive
977 evolution of the Moosfluh Landslide, Switzerland: Journal of Geophysical Research: Earth
978 Surface, v. 124, no. 12.
979 Grämiger, L. M., Moore, J. R., Gischig, V. S., Ivy-Ochs, S., and Loew, S., 2017, Beyond
980 debuttressing: Mechanics of paraglacial rock slope damage during repeat glacial cycles:
981 Journal of Geophysical Research-Earth Surface, v. 122, no. 4, p. 1004-1036.
982 Grämiger, L. M., Moore, J. R., Gischig, V. S., and Loew, S., 2018, Thermomechanical Stresses
983 Drive Damage of Alpine Valley Rock Walls During Repeat Glacial Cycles: Journal of
984 Geophysical Research-Earth Surface, v. 123, no. 10, p. 2620-2646.
985 Grämiger, L. M., Moore, J. R., Gischig, V. S., Loew, S., Funk, M., and Limpach, P., 2020,
986 Hydromechanical rock slope damage during Late Pleistocene and Holocene glacial cycles
987 in an Alpine valley: Journal of Geophysical Research: Earth Surface, v. 125, no. 8.
988 Groneng, G., Christiansen, H. H., Nilsen, B., and Blikra, L. H., 2011, Meteorological effects on
989 seasonal displacements of the Aknes rockslide, western Norway: Landslides, v. 8, no. 1,
990 p. 1-15.
991 Guglielmi, Y., Cappa, F., and Binet, S., 2005, Coupling between hydrogeology and deformation of
992 mountainous rock slopes: Insights from La Clapiere area (southern Alps, France):
993 Comptes Rendus Geoscience, v. 337, no. 13, p. 1154-1163.
994 Guglielmi, Y., Cappa, F., Rutqvist, J., Tsang, C. F., and Thoraval, A., 2008, Mesoscale
995 characterization of coupled hydromechanical behavior of a fractured-porous slope in
996 response to free water-surface movement: International Journal of Rock Mechanics and
997 Mining Sciences, v. 45, no. 6, p. 862-878.

998 Hansmann, J., Loew, S., and Evans, K. F., 2012, Reversible rock-slope deformations caused by
999 cyclic water-table fluctuations in mountain slopes of the Central Alps, Switzerland:
1000 Hydrogeology Journal, v. 20, no. 1, p. 73-91.
1001 Harper, J. T., Humphrey, N. F., Pfeffer, W. T., Fudge, T., and O'Neel, S., 2005, Evolution of
1002 subglacial water pressure along a glacier's length: Annals of Glaciology, Vol 40, 2005, v.
1003 40, p. 31-36.
1004 Hsieh, P. A., Bredehoeft, J. D., and Farr, J. M., 1987, Determination of aquifer transmissivity from
1005 Earth tide analysis: Water Resources Research, v. 23, no. 10, p. 1824-1832.
1006 Huang, D., Gu, D. M., Song, Y. X., Cen, D. F., and Zeng, B., 2018, Towards a complete
1007 understanding of the triggering mechanism of a large reactivated landslide in the Three
1008 Gorges Reservoir: Engineering Geology, v. 238, p. 36-51.
1009 Hubbard, B. P., Sharp, M. J., Willis, I. C., Nielsen, M. K., and Smart, C. C., 1995, Borehole Water-
1010 Level Variations and the Structure of the Subglacial Hydrological System of Haut Glacier
1011 Darolla, Valais, Switzerland: Journal of Glaciology, v. 41, no. 139, p. 572-583.
1012 Hugentobler, M., Aaron, J., and Loew, S., 2021, Rock slope temperature evolution and
1013 micrometer-scale deformation at a retreating glacier margin: under review at Journal of
1014 Geophysical Research-Earth Surface, v. Manuscript #2021JF006195.
1015 Hugentobler, M., Loew, S., Aaron, J., Roques, C., and Oestreicher, N., 2020, Borehole monitoring
1016 of thermo-hydro-mechanical rock slope processes adjacent to an actively retreating
1017 glacier: Geomorphology, v. 362, p. 107190.
1018 Iken, A., Fabri, K., and Funk, M., 1996, Water storage and subglacial drainage conditions inferred
1019 from borehole measurements on Gornergletscher, Valais, Switzerland: Journal of
1020 Glaciology, v. 42, no. 141, p. 233-248.
1021 Jennings, K. S., Winchell, T. S., Livneh, B., and Molotch, N. P., 2018, Spatial variation of the rain–
1022 snow temperature threshold across the Northern Hemisphere: Nature Communications, v.
1023 9, no. 1, p. 1148.
1024 Kaehler, C. A., and Hsieh, P. A., 1994, Hydraulic properties of a fractured-rock aquifer, Lee Valley,
1025 San Diego County, California, Washington, United States Government Printing Office,
1026 Geological survey water-supply paper 2394.
1027 Kirchner, J. W., 2009, Catchments as simple dynamical systems: Catchment characterization,
1028 rainfall-runoff modeling, and doing hydrology backward: Water Resources Research, v.
1029 45, no. 2.
1030 Kos, A., Amann, F., Strozzi, T., Delaloye, R., von Ruette, J., and Springman, S., 2016,
1031 Contemporary glacier retreat triggers a rapid landslide response, Great Aletsch Glacier,
1032 Switzerland: Geophysical Research Letters, v. 43, no. 24, p. 12466-12474.
1033 Krietsch, H., Gischig, V. S., Doetsch, J., Evans, K. F., Villiger, L., Jalali, M., Valley, B., Löw, S.,
1034 and Amann, F., 2020, Hydromechanical processes and their influence on the stimulation
1035 effected volume: observations from a decameter-scale hydraulic stimulation project: Solid
1036 Earth, v. 11, no. 5, p. 1699-1729.
1037 Lappegard, G., Kohler, J., Jackson, M., and Hagen, J. O., 2006, Characteristics of subglacial
1038 drainage systems deduced from load-cell measurements: Journal of Glaciology, v. 52, no.
1039 176, p. 137-148.
1040 Lavoine, E., Davy, P., Darcel, C., and Munier, R., 2020, A Discrete Fracture Network Model With
1041 Stress-Driven Nucleation: Impact on Clustering, Connectivity, and Topology: Frontiers in
1042 Physics, v. 8, no. 9.
1043 Loew, S., Gschwind, S., Gischig, V., Keller-Signer, A., and Valenti, G., 2017, Monitoring and early
1044 warning of the 2012 Preonzo catastrophic rockslope failure: Landslides, v. 14, no. 1, p.
1045 141-154.

Maillot, J., Davy, P., Le Goc, R., Darcel, C., and de Dreuzy, J. R., 2016, Connectivity, permeability, and channeling in randomly distributed and kinematically defined discrete fracture network models: Water Resources Research, v. 52, no. 11, p. 8526-8545.

Manga, M., Beresnev, I., Brodsky, E. E., Elkhoury, J. E., Elsworth, D., Ingebritsen, S. E., Mays, D. C., and Wang, C.-Y., 2012, Changes in permeability caused by transient stresses: Field observations, experiments, and mechanisms: Reviews of Geophysics, v. 50, no. 2.

Manning, C. E., and Ingebritsen, S. E., 1999, Permeability of the continental crust: Implications of geothermal data and metamorphic systems: Reviews of Geophysics, v. 37, no. 1, p. 127-150.

Marwan, N., 2020, Windowed Cross Correlation (corrgram), (https://www.mathworks.com/matlabcentral/fileexchange/15299-windowed-cross-correlation-corrgram), MATLAB Central File Exchange. Retrieved April 2020.

McColl, S. T., 2012, Paraglacial rock-slope stability: Geomorphology, v. 153-154, p. 1-16.

McColl, S. T., and Davies, T. R. H., 2013, Large ice-contact slope movements: glacial buttressing, deformation and erosion: Earth Surface Processes and Landforms, v. 38, no. 10, p. 1102-1115.

McColl, S. T., Davies, T. R. H., and McSaveney, M. J., 2010, Glacier retreat and rock-slope stability: debunking debuttressing, *in* Williams, A. L., Pinches, G. M., Chin, C. Y., McMorran, T. J., and Massey, C. I., eds., 11th Congress of the International Association for Engineering Geology and the Environment: Auckland, Aotearoa, Boca Raton, FL, United States: CRC Press, p. 467-474.

McColl, S. T., and Draebing, D., 2019, Rock Slope Instability in the Proglacial Zone: State of the Art, *in* Heckmann, T., and Morche, D., eds., Geomorphology of Proglacial Systems: Cham, Springer International Publishing, p. 119-140.

McMillan, T. C., Rau, G. C., Timms, W. A., and Andersen, M. S., 2019, Utilizing the Impact of Earth and Atmospheric Tides on Groundwater Systems: A Review Reveals the Future Potential: Reviews of Geophysics, v. 57, no. 2, p. 281-315.

Prager, C., Zangerl, C., Patzelt, G., and Brandner, R., 2008, Age distribution of fossil landslides in the Tyrol (Austria) and its surrounding areas: Natural Hazards and Earth System Sciences, v. 8, no. 2, p. 377-407.

Preisig, G., Eberhardt, E., Smithyman, M., Preh, A., and Bonzanigo, L., 2016, Hydromechanical Rock Mass Fatigue in Deep-Seated Landslides Accompanying Seasonal Variations in Pore Pressures: Rock Mechanics and Rock Engineering, v. 49, no. 6, p. 2333-2351.

Rahi, K. A., and Halihan, T., 2013, Identifying Aquifer Type in Fractured Rock Aquifers using Harmonic Analysis: Groundwater, v. 51, no. 1, p. 76-82.

Riva, F., Agliardi, F., Amitrano, D., and Crosta Giovanni, B., 2017, Damage-Based Time-Dependent Modeling of Paraglacial to Postglacial Progressive Failure of Large Rock Slopes: Journal of Geophysical Research: Earth Surface, v. 123, no. 1, p. 124-141.

Rouyet, L., Kristensen, L., Derron, M. H., Michoud, C., Blikra, L. H., Jaboyedoff, M., and Lauknes, T. R., 2017, Evidence of rock slope breathing using ground-based InSAR: Geomorphology, v. 289, p. 152-169.

Schulson, E. M., 1990, The brittle compressive fracture of ice: Acta Metallurgica et Materialia, v. 38, no. 10, p. 1963-1976.

Singhal, B. B. S., and Gupta, R. P., 2010, Applied Hydrogeology of Fractured Rocks, Dordrecht, Springer.

Spreafico, M. C., Sternai, P., and Agliardi, F., 2020, Paraglacial rock-slope deformations: sudden or delayed response? Insights from an integrated numerical modelling approach: Landslides.

Steck, A., 2011, 1269 Aletschgletscher mit Teil von 1249 Finsteraarhorn: Geolog. Atlas der Schweiz 1:25000.

1096 Stock, G. M., Martel, S. J., Collins, B. D., and Harp, E. L., 2012, Progressive failure of sheeted
1097 rock slopes: the 2009–2010 Rhombus Wall rock falls in Yosemite Valley, California, USA:
1098 Earth Surface Processes and Landforms, v. 37, no. 5, p. 546-561.
1099 Strozzi, T., Delaloye, R., Kaab, A., Ambrosi, C., Perruchoud, E., and Wegmuller, U., 2010,
1100 Combined observations of rock mass movements using satellite SAR interferometry,
1101 differential GPS, airborne digital photogrammetry, and airborne photography
1102 interpretation: Journal of Geophysical Research-Earth Surface, v. 115, no. F1.
1103 Styles, T. D., Coggan, J. S., and Pine, R. J., 2011, Back analysis of the Joss Bay Chalk Cliff Failure
1104 using numerical modelling: Engineering Geology, v. 120, no. 1, p. 81-90.
1105 Sugiyama, S., and Gudmundsson, G. H., 2004, Short-term variations in glacier flow controlled by
1106 subglacial water pressure at Lauteraargletscher, Bernese Alps, Switzerland: Journal of
1107 Glaciology, v. 50, no. 170, p. 353-362.
1108 Theis, C. V., 1935, The relation between the lowering of the Piezometric surface and the rate and
1109 duration of discharge of a well using ground-water storage: Eos, Transactions American
1110 Geophysical Union, v. 16, no. 2, p. 519-524.
1111 Van Camp, M., and Vauterin, P., 2005, Tsoft: graphical and interactive software for the analysis
1112 of time series and Earth tides: Computers & Geosciences, v. 31, no. 5, p. 631-640.
1113 Welch, L. A., and Allen, D. M., 2014, Hydraulic conductivity characteristics in mountains and
1114 implications for conceptualizing bedrock groundwater flow: Hydrogeology Journal, v. 22,
1115 no. 5, p. 1003-1026.
1116 Wolter, A., Roques, C., Gröble, J., Ivy-Ochs, S., Christl, M., and Loew, S., 2020, Integrated multi-
1117 temporal analysis of the displacement behaviour and morphology of a deep-seated
1118 compound landslide (Cerentino, Switzerland): Engineering Geology, v. 270, p. 105577.
1119 Wolters, G., and Müller, G., 2008, Effect of Cliff Shape on Internal Stresses and Rock Slope
1120 Stability: Journal of Coastal Research, v. 2008, no. 241, p. 43-50.
1121 Wyllie, D. C., and Mah, C. W., 2004, Rock slope engineering: civil and mining, Taylor & Francis.
1122 Young, A. P., and Ashford, S. A., 2008, Instability investigation of cantilevered seacliffs: Earth
1123 Surface Processes and Landforms, v. 33, no. 11, p. 1661-1677.
1124 Zhou, X., 2008, Determination of aquifer parameters based on measurements of tidal effects on
1125 a coastal aquifer near Beihai, China: Hydrological Processes, v. 22, no. 16, p. 3176-3180.

1126